International Journal of Greenhouse Gas Control 66 (2017) 230–245

Contents lists available at ScienceDirect

International Journal of Greenhouse Gas Control

journal homepage: www.elsevier.com/locate/ijggc

Visualization and prediction of supercritical CO_2 distribution in sandstones during drainage: An *in situ* synchrotron X-ray micro-computed tomography study

Marco Voltolini[a], Tae-Hyuk Kwon[b], Jonathan Ajo-Franklin[a,*]

[a] Lawrence Berkeley National Laboratory, Berkeley, CA, USA
[b] Korea Advanced Institute of Science and Technology, Daejeon, South Korea

ARTICLE INFO

Keywords:
Geological carbon sequestration
$scCO_2$ drainage
In situ synchrotron X-ray micro computed tomography
3D quantitative morphometric analysis
Drainage predictive model.

ABSTRACT

Pore-scale distribution of supercritical CO_2 ($scCO_2$) exerts significant control on a variety of key hydrologic as well as geochemical processes, including residual trapping and dissolution. Despite such importance, only a small number of experiments have directly characterized the three-dimensional distribution of $scCO_2$ in geologic materials during the invasion (drainage) process. We present a study which couples dynamic high-resolution synchrotron X-ray micro-computed tomography imaging of a $scCO_2$/brine system at *in situ* pressure/temperature conditions with quantitative pore-scale modeling to allow direct validation of a pore-scale description of $scCO_2$ distribution. The experiment combines high-speed synchrotron radiography with tomography to characterize the brine saturated sample, the $scCO_2$ breakthrough process, and the partially saturated state of a sandstone sample from the Domengine Formation, a regionally extensive unit within the Sacramento Basin (California, USA). The availability of a 3D dataset allowed us to examine correlations between grains and pores morphometric parameters and the actual distribution of $scCO_2$ in the sample, including the examination of the role of small-scale sedimentary structure on CO_2 distribution. The segmented $scCO_2$/brine volume was also used to validate a simple computational model based on the local thickness concept, able to accurately simulate the distribution of $scCO_2$ after drainage. The same method was also used to simulate Hg capillary pressure curves with satisfactory results when compared to the measured ones. This predictive approach, requiring only a tomographic scan of the dry sample, proved to be an effective route for studying processes related to CO_2 invasion structure in geological samples at the pore scale.

1. Introduction

Geological carbon sequestration (GCS), the injection and storage of carbon dioxide in a supercritical phase ($scCO_2$) into the deep subsurface, is one of several scalable approaches for mitigating atmospheric emissions from large point sources of CO_2 (IPCC special report, 2005). One key to the efficacy of GCS is an understanding of both early injection dynamics and storage permanence, largely controlled by a variety of trapping mechanisms which prevent leakage of the buoyant CO_2 phase into ground water aquifers located closer to the surface. The primary trapping mechanisms considered in contemporary models are, in order of security and required time: i) stratigraphic trapping, where CO_2 is trapped by impermeable rocks above the injection interval; ii) capillary trapping, where $scCO_2$ is immobilized by capillary forces at the pore scale; iii) dissolution trapping, where $scCO_2$ eventually dissolves in the formation brine; iv) mineral trapping, where aqueous CO_2 reacts with formation minerals to yield carbonates. These processes are not independent and happen simultaneously from the initial phases of injection with early periods dominated by stratigraphic trapping followed by capillary trapping during plume movement, dissolution, and eventual mineralization. The present work focuses on the $scCO_2$ invasion process, also referred to as drainage, given its importance as the first step toward CO_2 storage in many targeted reservoirs.

Early in the lifetime of a plume, injected $scCO_2$ displaces formation brine, a process which generates an initial CO_2 distribution geometry at the pore- to meso-scale. The characteristic geometry of this initial CO_2 distribution controls a variety of processes ranging from CO_2 dissolution rates (through variations in brine/CO_2 interfacial area) to the seismic response of rocks partially saturated with CO_2 via “patchy” saturation effects (e.g. White, 1975, Caspari et al., 2011; Nakagawa, 2011; Rubino et al., 2011; Ajo-Franklin et al., 2013). This initial invasion process is controlled by competition between viscous, capillary, and buoyant forces and hence is sensitive to pore dimensions, surface wettability, fluid viscosities, fluid densities, interfacial tension, and

* Corresponding author.

http://dx.doi.org/10.1016/j.ijggc.2017.10.002
Received 6 March 2017; Received in revised form 3 October 2017; Accepted 11 October 2017
Available online 21 October 2017

injection rates. A variety of studies in analog systems of two immiscible fluids, particularly of optically transparent 2D granular systems at low pressures, have found that this initial distribution can be described by invasion-percolation (IP) theory (e.g. Wilkinson and Willemsen 1983), assuming sufficiently low flow rates where capillary forces dominate the drainage process, e.g. capillary numbers of less than 10^{-6} (see experiments of Cinar et al., 2007; Chalbaud et al., 2009; Toussaint et al., 2012). In such pore-scale IP models, the drainage proceeds through sequential displacement of the wetting fluid in sequence of lowest capillary entry pressures. Assuming low formation heterogeneity, the local flow rate (and hence capillary number) scales with radial distance from an injection well and injection rate. Therefore, capillary numbers of these magnitudes can be generally expected in a variety of realistic GCS scenarios at distances greater than 10 m from the wellbore. To describe the drainage and the two-phase flow in general, a number of different models have been developed, because of the importance of this process for the oil and gas exploitation as well as geological carbon storage. Examples range from the early development of continuum models before the advent of automated computation (e.g. Muskat and Meres, 1936; Wyckoff and Botset, 1936) to modern pore-scale models developed for two-phase flow in reservoir rocks (e.g. Blunt and King, 1991; Bryant and Blunt, 1992; Bakke and Øren, 1997; Patzek, 2000; Øren and Bakke, 2003; Steefel et al., 2013).

To date, relatively few studies have attempted to directly visualize brine/$scCO_2$ systems at the pore scale and test pore-resolved numerical models of drainage, largely due to the difficult nature of imaging pore-scale CO_2 distribution at high pressures in actual rock samples, as well as the challenges of directly modeling multi-phase flow at the pore scale over large modeling domains (e.g. Meakin and Tartakovsky, 2009; Blunt et al., 2013). Over the last decade, X-ray micro-Computed Tomography (μCT) has been effectively used for experimentally obtaining the distribution of $scCO_2$ in reservoir rock samples (e.g. Silin et al., 2011; Iglauer et al., 2011; Andrew et al., 2013, 2014a,b; Andrew et al., 2015; Herring et al., 2014). However, the full sample modeling of the $scCO_2$ drainage process using the true pore morphology, at the micrometer scale, has yet to be validated against one of the described datasets. Silin et al. (2011) showed a small sub-sample demonstration of the maximum inscribed sphere (MIS) + IP approach, previously explored by Silin and Patzek (2006), and validated the resulting distribution against an imaged section of a sandstone sample. However, this pioneering effort was complicated by low image quality and phase contrast artifacts which made 3-phase segmentation and image analysis quite challenging; this resulted in limitations in both modeled volumes and reproduction of imaged $scCO_2$ distribution. Setting aside Silin and his co-workers' effort, the previously described experimental studies (e.g. Iglauer et al., 2011; Andrew et al., 2014; Herring et al., 2014) have placed an emphasis on statistical and morphological analysis of $scCO_2$ distribution (e.g. cluster analysis) rather than predictive modeling of pore-scale distribution of the non-wetting phase. These previous studies also do not consider the role of macroscopic heterogeneities, including depositional features, on pore-scale $scCO_2$ distribution by choosing relatively homogeneous samples e.g. the Frio sand (Silin et al., 2010) and Ketton limestone (Iglauer et al., 2011; Andrew et al., 2014). However, realistic maps of $scCO_2$ distribution in natural heterogeneous sandstones (e.g. with significant heterogeneity) have not been acquired to date, and moreover, the prediction of $scCO_2$ distribution via pore-scale modeling using natural rock-pore morphology has been rarely attempted.

In this study, we seek to combine high-resolution *in situ* synchrotron X-ray μCT imaging of the $scCO_2$ drainage process with a modification of Silin's MIS-IP approach to quantitatively test the predicted $scCO_2$ distribution at the pore scale (resolution at the micrometer scale) on mini-cores (~1 cm in diameter). To enable this study, we designed and fabricated an X-ray transparent high-pressure triaxial cell suitable for *in situ* pressure (P) and temperature (T) conditions, both necessary for replicating the physical characteristics of $scCO_2$. The combined use of high-speed radiography and μCT allowed us to effectively capture both the rapid invasion distribution and the quasi-static pore-scale distribution of the $scCO_2$ phase. The porous medium sample selected for our study is a high permeability sandstone from the Domengine formation which is a current GCS target in California's Sacramento Basin and a prolific conventional dry gas reservoir near Rio Vista, CA (USA). It is worth emphasizing that many studies in this field of research do not use actual candidates rocks for geological sequestration and instead focus on either synthetic aggregates (such as packed glass beads, clean quartz grains, etc.) or "standard" homogeneous sandstones (e.g. Berea) to minimize difficulties caused by sample heterogeneity. Besides the relevance of the Domengine formation as a potential $scCO_2$ injection target, the presence of mm-scale depositional features allowed analysis of the role of sorting variations on $scCO_2$ distribution during drainage. We quantitatively evaluate the MIS-IP pore-scale $scCO_2$ distribution predictions against the measured distribution; the comparison reveals an excellent saturation match with the primary differences resulting from replication of boundary conditions. The good match extends to pore-scale occupancy and small features at the interfacial scale. We also use the same approach to model capillary pressure curves and the resulting predictions fit measured Hg porosimetry results on the same samples. We believe this approach, now validated, will provide a computationally efficient path to estimating pore-scale $scCO_2$ distributions during drainage, given rock micro-structure and boundary conditions, a critical component of estimating mesoscale hydrologic, geochemical, and seismic properties during injection.

2. Experimental

2.1. Sandstone sample selection

As mentioned previously, a sandstone core obtained from the Domengine formation was used in this study. A 63.5-mm-long sandstone core was collected from a gallery at Black Diamond Mine Regional Park (Antioch, CA, United States) from the Hazel-Atlas Mine, from which a sub-core, with a diameter of 9.5 mm and a length of 20 mm, was obtained to provide a cylindrical sample of a proper size for the X-ray μCT imaging. The Domengine formation is a regionally extensive sandstone unit with significant natural gas production (Rio Vista, CA); the Domengine, particularly the near-shore facies, often possesses excellent reservoir characteristics including high porosities and permeabilities. At present, the Domengine is considered one of several regional targets for geological CO_2 sequestration in the Sacramento Basin in areas where the formation is present at sufficient depth. The Domengine member considered in this study, the Ione (Cherven, 1983), is a sandstone mainly composed of rounded quartz grains with minor amounts of feldspars and clay. A Rietveld analysis of a X-ray Powder Diffraction profile measured from a sample taken from the starting material gave the following result [weight% (sigma)]: quartz 73.8(3), K-feldspar 22.7(4), smectite 3.5(2), consistent with a typical quartz-rich sandstone.

2.2. HP/HT system design & realization

The primary challenge restricting visualization of multiphase flows at elevated pressures and temperatures is the development of pressure vessels with sufficiently low X-ray opacity to allow imaging. Our miniaturized triaxial vessel (fabricated by *CoreTest Systems*, CHHS-128Z), made of a high strength aluminum alloy (Al 7075-T651), was designed to target *in situ* pressure and temperature (PT) conditions compatible with most of the GCS pilot sites, with a maximum allowable working pressure of 24.1 MPa (3500 psi) at temperatures up to 60 °C. To match the appropriate combination of CO_2 density and viscosity with *in situ* conditions, PT conditions must be beyond the critical point of CO_2 (7.38 MPa, 33.1 °C); additionally, some distance from the critical point in PT space is desirable to eliminate a high sensitivity of CO_2 properties

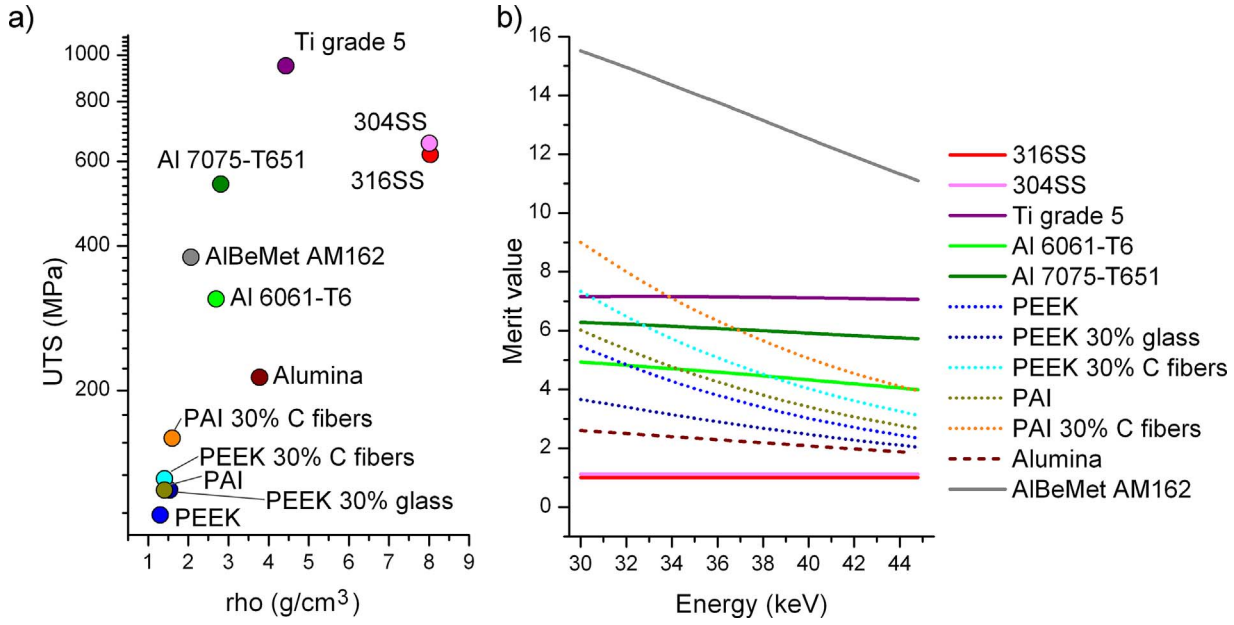

Fig. 1. Plots showing properties relevant to the construction of the outer shell of the HP/T cell. In (a) the Ultimate Tensile Strength (UTS) vs. Density (ρ) (used as a proxy for X-ray transparency) is shown. In (b) a merit function related to strength and linear absorption coefficient vs. X-ray energy for the different materials (alloys: solid lines, plastics and composites: dotted, ceramics: dashed) is shown. It is clear how the performance of plastics become less and less appealing when increasing the X-ray energy and the varied performance of the different alloys.

to small perturbations in conditions during experimental operations.

Classical high pressure (HP) systems are typically manufactured from alloys of stainless steel (e.g. 316SS, 304SS) or titanium, two materials with very low X-ray transparency at the energies available at the synchrotron facility selected for our experiment, the Beamline (BL) 8.3.2 at the Advanced Light Source (ALS) located in Berkeley, CA (USA). An HP system aimed at X-ray imaging has some specific additional requirements: it must be compact enough to be mounted on the sample stage (and allow at least a 180° rotation) and the part of the cell accommodating the sample along the X-ray beam needs to be sufficiently transparent to X-rays over the entire scan angle. The main challenge in the selection of the proper material for building this kind of cell is to find the best compromise between X-ray attenuation, strength, workability, safety, and cost. Concerning X-ray transparency and strength, useful metrics in material selection include ultimate tensile strength, density and linear absorption coefficients at different energies, to better estimate the absorption properties of the materials. The main materials considered and their properties are summarized in Fig. 1 where the density (ρ) is plotted against the ultimate tensile strength (UTS) in Fig. 1a. Two subgroups for polymers and metals are clearly recognizable, but a choice based on this plot alone would be difficult. After calculating the linear absorption coefficient μ for the hard X-ray spectrum available at the beamline and plotting a merit value = UTS/μ^2 normalized with respect the 316SS chosen as a "standard" reference material, some further observations can be made, as shown in Fig. 1b. Beyond tensile strength and density (a proxy for X-ray opacity), the secondary constraints in material selection include machinability (low for ceramics), health and safety hazards during fabrication (high for Be- and Mg- based alloys), susceptibility to X-ray damage, temperature performance, failure modes, and cost. Be alloys, while excellent from a strength/opacity perspective, present significant machining and utilization hazards due to Be dust exposure. Grade 5 Titanium presents the best strength/density ratio but during preliminary tests was too attenuating to allow efficient imaging at thickness values considered safe. Among the materials considered, a mid-Cu aluminum alloy (Al 7075-T651) was selected as the most appropriate for engineering our imaging cell. Al 7075-T651 has a high tensile strength (538 MPa at room temperature), is easy to machine, of moderate cost, fails in ductile fashion, and is relatively transparent to X-rays at 30–40 keV. Not considered during our design studies were carbon fiber composite vessels due to lack of data concerning X-ray damage to fiber epoxy encapsulations; despite this issue, such systems may provide advantages from a strength/opacity perspective and should not be dismissed in future design studies.

The resulting system is a miniature version of a traditional triaxial core flood system with independent axial and confining loads applied with a top piston and a flexible jacket respectively, as shown in Fig. 2. Fluid injection ports on both the top (2 ports) and bottom (1 port) of the system allow push/pull or in-sample mixing experiments. A thermistor was housed and attached on the sample jacket via electrical feedthroughs to monitor sample temperature. The vessel can be bolted to the top leaflet of a kinematic mounting system (Newport Optics) to allow micrometer repeatability if off-line experiments with repeated imaging are needed. The vessel was sized for cylindrical samples of approximately 9.525 mm (3/8 in) wide and 19.05 mm tall (3/4 in); these dimensions were deemed the most appropriate for mid-resolution pore-scale imaging at ALS BL 8.3.2 (4.4 μm/voxel) while simultaneously providing sufficient sample size to generate a volume with a good degree of representativeness for continuum analysis.

2.3. Protocol during experimental run

The miniature triaxial system was utilized during a series of $scCO_2$ drainage and imbibition experiments carried out at ALS BL 8.3.2. During the experiments described in this paper, confining and axial pressure were maintained by a single high-pressure syringe pump (ISCO-Teledyne 260HP) operating in constant pressure mode; fluid injection during drainage and imbibition were carried out using a pair of high-pressure syringe pumps (ISCO-Teledyne 500HP) configured to operate in a push/pull fashion. The injector pump operated in a constant flow-rate mode while the withdrawal pump was operated in constant back-pressure mode. Injection, extraction, and confining pressures were continuously logged using a set of pressure transducers (Ashcroft Instruments); temperature was also continuously monitored using a thermistor installed within the vessel on the jacket exterior as well as K-type thermocouples in the experimental hutch, in the

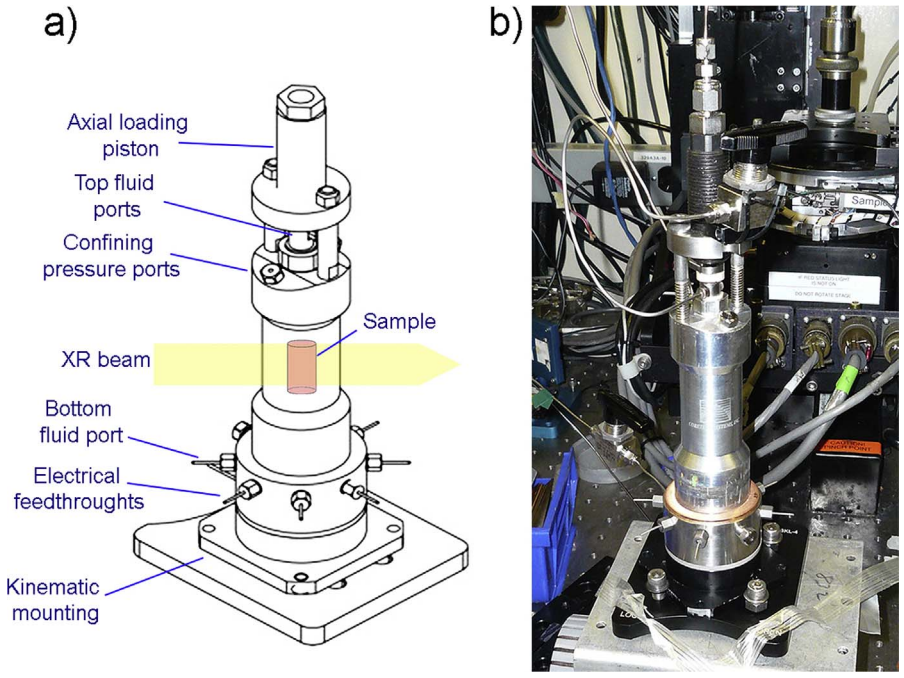

Fig. 2. a) Schematics of the HP flow cell with the most important features labeled. b) Photograph of the cell before an in-situ flow-through experiment with $scCO_2$.

injection line, and attached to the exterior of the vessel. Distilled (DI) water was used as the pressure medium for both confining and axial pressures. Injection and sample temperature were controlled by a circulating unit fed to a tight circuit of thin Tygon® tubing encapsulating the top and bottom sections of the input line and vessel.

The sandstone sample was prepared by initial immersion in a large volume of DI water to remove any precipitated salts from the partially saturated mine environment and then dried for 48 h at 40 °C in a convection oven. The sample was jacketed using a 1 mm thick Viton® jacket, sealed against the exterior confining pressure by way of a thin stainless wire clamp. The vessel was then pressurized to 4.1 MPa (600 psi) and, after repeating the flushing of the sample with low-pressure CO_2 gas three times, the sample was flooded with 0.1 M brine consisting only of distilled degassed H_2O and potassium iodide (KI, Sigma Aldrich). The brine injection was conducted at 1.4 MPa (200 psi) and 0.4 ml/min until 20 pore volumes had been injected. Thereafter, the confining and pore pressures were increased to 10.7 MPa (1550 psi) and 8.8 MPa (1273 psi) respectively and another 20 pore volumes of the degassed KI brine were circulated to achieve a brine-saturated condition, removing any trapped gas. At this point, the interior temperature of the vessel was set at ~44 °C as measured by the internal thermistor. Ultra-high purity CO_2 was then introduced into the injection pump at 4.8 MPa (700 psi) and pressurized to 8.8 MPa (1270 psi). In spite of the internal temperature of the hutch (~25 °C), owing to the sufficiently low flow rate, the injected the CO_2 was heated to a supercritical state (~44 °C, 8.8 MPa) during the passage through the heated segment of the vessel before entering the sample, as confirmed by the inside thermistor attached to the jacket. The initial drainage experiment ($scCO_2$ injection) was conducted at these conditions and a flow rate of 0.001 ml/min as measured at the injection pump. Initial $scCO_2$ capillary invasion into the sandstone sample was monitored with high-speed multi-tile radiography. Once the $scCO_2$ breakthrough into the sample was observed, a tomographic scan of the sample was acquired at such a partially brine-saturated state.

2.4. Synchrotron X-ray microtomography (SXR-μCT) acquisition and reconstruction

As mentioned previously, all dynamic μCT imaging was performed at the ALS, BL 8.3.2, a flexible imaging facility for characterizing the microstructural attributes of mid-sized (< 1 cm) samples down to sub-μm resolutions. The details of the beamline, which operates on a superconducting bend magnet (11.5 keV critical energy), are described in MacDowell et al. (2012). Recent studies at BL 8.3.2 have explored a variety of problems related to the pore-scale coupling of structure, hydrogeology, and geochemistry (e.g., Wu et al., 2011; Armstrong and Ajo-Franklin, 2011; Noiriel et al., 2012; Landrot et al., 2012; Kneafsey et al., 2013).

From an imaging perspective, the experiments described in the publications cited above were challenging because the beam available at ALS BL 8.3.2 is relatively soft compared to other hard X-ray imaging synchrotron imaging facilities. The X-ray beam must penetrate the aluminum alloy vessel shell, the water annulus used for confinement, the Viton jacket, and the sample itself, saturated with an attenuating fluid (0.1 or 0.25 M KI). To maintain high signal to noise ratio and fast acquisition time, all experiments were conducted using the polychromatic X-ray beam directly from the insertion device, pre-hardened using a 3 mm Al 6061 filter in the beam path. The filter cut the low energy X-ray of the spectrum by means of absorption, minimizing beam-hardening issues in the reconstructed data, and also prevented uncontrolled vessel heating while maintaining sufficient flux for timely data acquisition. Beam-hardening effects on the sample with this configuration are minimized by the combination of the resulting hardness of the XR with the outer layers of the sample (cell wall, confining fluid), further absorbing the lower energy spectrum of the incident X-ray beam. The detector system was configured with a Ce-doped YAG scintillator and a 2× optical objective (Mitutoyo) to yield a voxel size of 4.4 μm (isotropic). The CCD detector utilized was a PCO-4000 (Cooke Corporation, 4008 × 2672 px) and all images were acquired without spatial binning.

Because the height of the sample exceeded the vertical field of view, the full sample was scanned as a sequence of 6 tiled acquisition with the vertical overlaps of ~40 pixels. During full tomography runs, scans were acquired with 1801 projections (0.1° increments) with interleaved flat field images to correct for beam structure variations during the scan. Sample to detector distance was ~25 cm for all the measurements. Exposure times varied from 80 ms (with sample) to 10 ms (flat field) and were adjusted to prevent CCD saturation. The experiment yielded a 3D tomographic dataset of the whole dry sample, radiographs of the full sample during the drainage process, and one tomographic

subvolume of the sample after the drainage.

2.5. Volume reconstruction procedure using a single-distance phase retrieval algorithm

The reconstruction of the volume was performed using two different procedures for the baseline measurement of the whole sample and for the section of the sample measured after the $scCO_2$ invasion, given the different characteristics of the datasets: the baseline only had two phases to be segmented characterized by very different X-ray attenuation values (sand and gas), while the volume after invasion had three different phases with more similar X-ray attenuation values (sand, KI brine, and $scCO_2$) The baseline volume was reconstructed using a standard filtered backprojection algorithm, using a Shepp-Logan filter (Kak and Slaney, 1987), applied to the flat-field corrected projections. This approach provided datasets that were easy to segment. When the same procedure was applied to the dataset with the $scCO_2$, the separation of the three main phases (sand grains, brine, and $scCO_2$) was more difficult, with the high noise levels making the attenuation values (i.e. the resulting grayscale of the dataset) of the different phases significantly overlap. This problem was further aggravated by phase contrast artifacts generated by the high spatial coherence of the beam. To improve the data quality, we applied a single-distance phase retrieval algorithm to the projections, since this generally provides data with a better separation of gray levels corresponding to different materials, improving the signal-to-noise ratio. The same approach also reduces phase contrast artifacts, aiding significantly in the thresholding process needed for the binarization of the dataset, prior to morphometric and textural analysis. The slight smoothing effect of the phase retrieval procedure was also useful in suppressing noise and weakening the thinner ring artifacts present in the original dataset.

The single-distance algorithm proposed by Paganin et al. (2002) and implemented in the ANKAphase software package (Weitkamp et al., 2011) was chosen for phase retrieval. During the experiment, filtered ("hardened") synchrotron polychromatic light was used for the measurement, and the sample-detector distance was set in order to be in the near field of the Fresnel diffraction region (e.g. Bronnikov, 2002). While Paganin's algorithm has been theoretically developed for monochromatic radiation and monophase low-attenuating samples, deviations from the theory (both for polychromaticity and composition) are often tolerated, whilst providing semi-quantitative results. This issue is discussed in more detail in Meyers et al. (2007) and Weitkamp et al. (2011), where theoretical explanations as well as real examples are provided. The parameters used for the phase retrieval were: $\beta/\delta = 0.49$, sample-detector distance = 25 cm, and energy = 28 keV. After applying phase retrieval to the projections, the reconstruction was performed using a conventional filtered backprojection algorithm with the Octopus software (Dierick et al., 2004), in the same fashion as for the baseline dataset.

In Fig. 3, the differences on a detail of the sample after the reconstruction with (bottom row) and without (top row) phase retrieval are shown. The profiles in panel (a) show the effect of the phase retrieval algorithm across a brine/grain/$scCO_2$ boundary; note the overshoot in estimated attenuation due to phase contrast effects in the top section. As can be seen in panel (c), the grayscale histogram was strongly modified, and the effect of the phase contrast artifacts (one has been highlighted in yellow in the figure) were removed in the data reconstructed after phase retrieval, together with an increase in the signal-to-noise ratio, which allowed for an improved separation of the different phases.

3. Results: morphometric analysis of SXR-μCT baseline dataset

The volume data obtained from SXRμCT can be used for non-destructive visualization purposes (virtual cuts, etc.), but can also be used to obtain quantitative information concerning the structural characteristics of the sample. We performed a complete characterization of the morphology and texture of the baseline dataset (whole sample, dry scan) in order to explore any correlation existing between microstructural features and $scCO_2$ distribution, including correlation between local porosity, grain dimension, or pore throat size and zones of $scCO_2$ saturation.

3.1. Data reduction procedure on baseline SXR-μCT data

To carry out a comprehensive characterization of the microstructure of the sandstone core, different analytical strategies were applied to the dataset of the gas-saturated sandstone core, collected as a baseline prior to the injection of the $scCO_2$. Both the grain space and the pore space were considered during analysis. Generally, the first step in the preparation of a dataset prior to the morphometric analysis is the filtering of noise, to aid the following segmentation process. In the dataset presented in this work, the denoising procedure was performed using a 3D median filter, since it reasonably preserves the shape of the objects and is effective in removing "salt and pepper" noise. As a principle, filtering should be kept to a minimum to avoid changes in the shapes of the objects. This is particularly crucial in the presence of small (in the sense that they are described by a small number of voxels) objects; however, this group of datasets did not suffer from this issue because each sand grain – or pore – is generally described by at least hundreds of voxels. After filtering, the dataset was resampled to obtain a 8.8 μm voxel size, from the original 4.4 μm, to obtain a final volume of 919 × 919 × 2250 voxels; the large grain size in comparison to the voxel size made this step possible and the resulting downsampling greatly decreased computational costs during analysis.

Morphometric analysis requires that a binary volume be calculated first: a segmentation procedure is required to separate the sand grains from the pores. Among the large number of segmentation algorithms developed, it was found that the Otsu (Otsu, 1979) and IsoData (Ridler and Calvard, 1978) algorithms were in general the most accurate in separating pores from sand grains for this dataset, as evaluated by visual inspection of the results. In the results discussed, the Otsu algorithm as implemented in ImageJ was chosen for analysis.

Segmentation procedures are sensitive to noise and reconstruction artifacts. Because of the unavoidably complex experimental setup, the noise levels were high, and some ring artifacts were present even after application of a ring suppressor filter during the reconstruction procedure. Therefore, no direct thresholding procedure provided satisfactory results. In the cases of noisy image datasets, the use of heavy filtering, such as cycles of 3D Gaussian smoothing, or even edge-preserving filters, such as bilateral filtering (see Tomasi and Maduchi, 1998), impacts the shape of segmented objects to an unacceptable extent. Thus, a different and less invasive approach was developed.

A simple and very effective procedure, which often works well in samples with small/thin connected objects and sharp noise, is to apply a threshold and then extract the largest connected component. Such procedure preserve the shape of the connected volume and erase noise in other parts of the sample. This has been found to work well in connected frameworks, such as glass in volcanic rocks, as presented in Zandomeneghi et al. (2010), but in granular materials, where single grains can be isolated, some different procedures can be used to obtain better results. In the present dataset, we used a masking procedure: we performed a simple threshold on the original dataset to obtain a thresholded image with the noise, then we used another thresholded image to create a mask using 3D erosion and dilating cycles to eliminate the small voxel clusters and isolated voxels due to the noise. The objects in this mask were slightly larger than the original thresholded image (setting proper eroding-dilating parameters), free of noise, but with the shape of the objects too modified to be acceptable. An *AND* Boolean operation of the two datasets would provide a binary dataset mostly free of noise and with the original shape of the objects almost perfectly preserved. This procedure was found to be extremely useful when

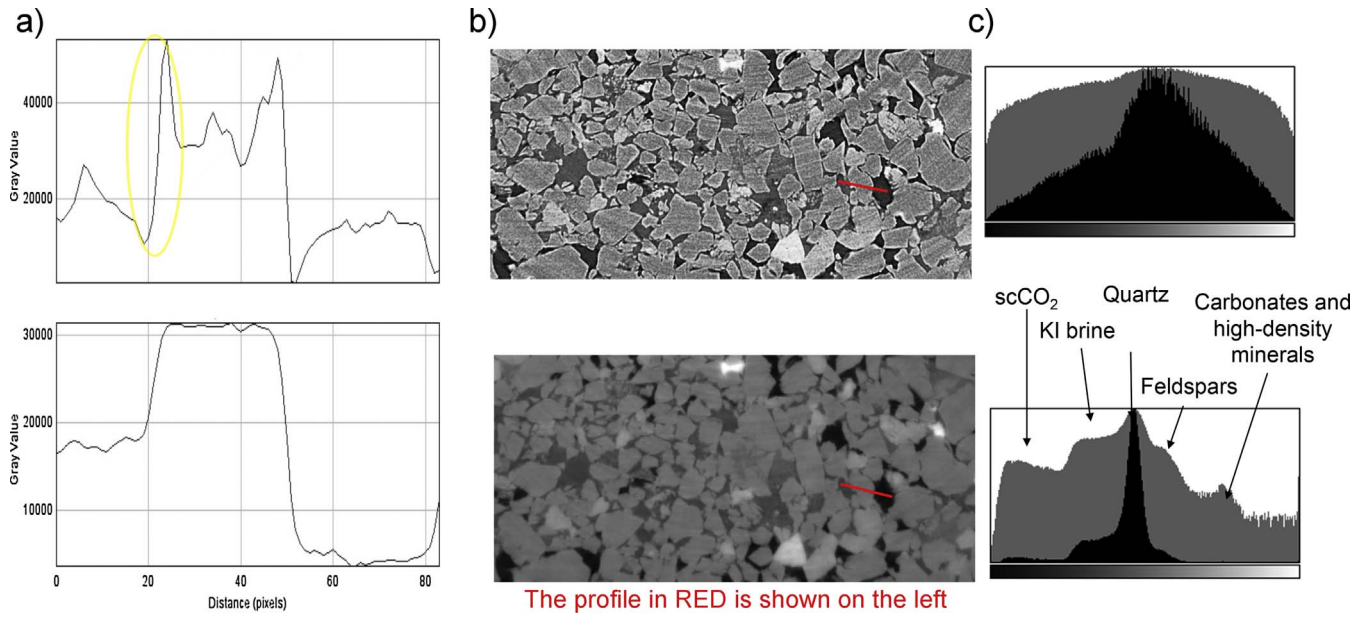

Fig. 3. Characteristics of the dataset before and after phase retrieval: both the profile (marked in red in the slice) and the gray level histograms show a significant improvement in the data quality (see text for more details). (For interpretation of the references to colour in this figure legend, the reader is referred to the web version of this article.)

thresholding objects with similar greylevels but totally different morphological characteristics (see again Zandomeneghi et al., 2010), being based on the shape and size of the objects. The results of this procedure, prior to the separation and morphometric analysis, are shown in Fig. 4, where a subvolume virtually cut from the original dataset is presented: on the top of the figure, a volume rendering of the subvolume and its binarized volume (the sand grains) is shown. In this case, it is possible to appreciate how the shapes are preserved and the low noise levels.

An advanced morphometric analysis requires the separation of different objects within a class: in our case we seek to separate individual sand grains within the sample to enable analysis of grain size and shape analysis. In granular materials, the usual approach to obtain this separation is a procedure based on the watershed algorithm (Meyer, 1994; Roerdink and Meijster, 2001). In the procedure used to separate the single sand grains in the dataset, a minima suppressor filter was applied to the calculated distance transform volume (e.g., Borgefors, 1996) in order to avoid overseparation during successive watershed iterations. The result after this procedure is shown in Fig. 4. To verify the results of the separation, a connected component labeling was conducted by assigning a corresponding different graylevel value to each separated sand grain (Hu et al., 2005) and visually comparing the different volumes. The image result after this labeling procedure is again shown in Fig. 4, where it is possible to appreciate the appropriate separation of individual sand grains.

To examine the sample heterogeneity, the full dataset was divided into 9 equal subvolumes (~2.2 mm tall) horizontally (following the layering present in the sample, also roughly horizontal), as shown in Fig. 5. Once the sand grains were separated, and the different binarized subvolumes were available, the morphometric analysis on the grain space was carried out. The main goal of this analysis was to quantitatively characterize the microstrucure of the rock, such that a range of different morphometric parameters were evaluated. Different morphometric parameters were calculated using Blob3D (Ketcham, 2005a), Fiji (Schindelin et al., 2012), and other customized procedures, as explained in detail in Section 3.2. Fig. 4 shows an example, where the grain size distribution and the sphere-normalized surface to volume ratio (SNSVR) histograms are plotted. From the orientation distribution function obtained from the sand grains in the subvolumes, it was possible to calculate pole figures showing the shape preferred orientation of the sand grains (the three axis of the ellipsoid fitting each object: ε_x, ε_y, ε_z as minimum, medium, and maximum axis, respectively), as shown at the bottom of Fig. 4.

3.2. Morphometric characteristics of grains

In Fig. 5 we present a global overview of the morphometric analysis results on the solid matrix (panel c) and the pore space (panel b). The volume rendering of the whole sample is shown with two different subvolumes shown in higher detail to emphasize the difference in grain size, highlighted by some horizontal bedding of coarser, or finer, grains within the sample (panel a). A slice-by-slice porosity plot is shown for reference as well. Histograms showing the variation of the different relevant grain morphometric parameters calculated in the different subvolumes are also presented; grains cut by the surface of the subvolumes are not considered for morphometric analysis. The number of grains provides information about the statistical significance of the analysis and provides indirect information about the volume and packing of the sand grains. Another fundamental parameter we calculate is the mean radius of the sand grains (i.e. the mean size of the single sand grains present in each subvolume), which is inversely related to the number of sand grains in the subvolumes, as expected. It is worth noting that the histograms in Fig. 5 show average data, but the complete distributions are available, as previously shown in Fig. 4. The SNSVR is an important parameter to investigate the shape and the characteristics of the surface of the objects: values close to 1 indicates shapes close to a sphere, with a smooth surface, while higher values would indicate more irregular shapes with large surface areas. This is a key parameter for quantification in reactive systems where it can be used to improve surface area estimates. The average aspect-ratio (AR) is another parameter useful to describe the shape of the objects, leading to preferred orientation that can cause anisotropy, e.g. in flow properties. To examine the anisotropy present in the sand grain population, a single object-oriented approach was used, as presented in Voltolini et al. (2011). We calculated the texture index F_2 which is 1 for a random distribution and $+\infty$ for perfectly iso-oriented objects (Bunge, 1982). It is observed that the preferred orientation is related to the aspect ratio, but the overall anisotropy of this sample is extremely weak with little variation among the different subvolumes.

With regards to the statistical properties of the grain matrix, our primary observation was the presence of mm to sub-mm laminations

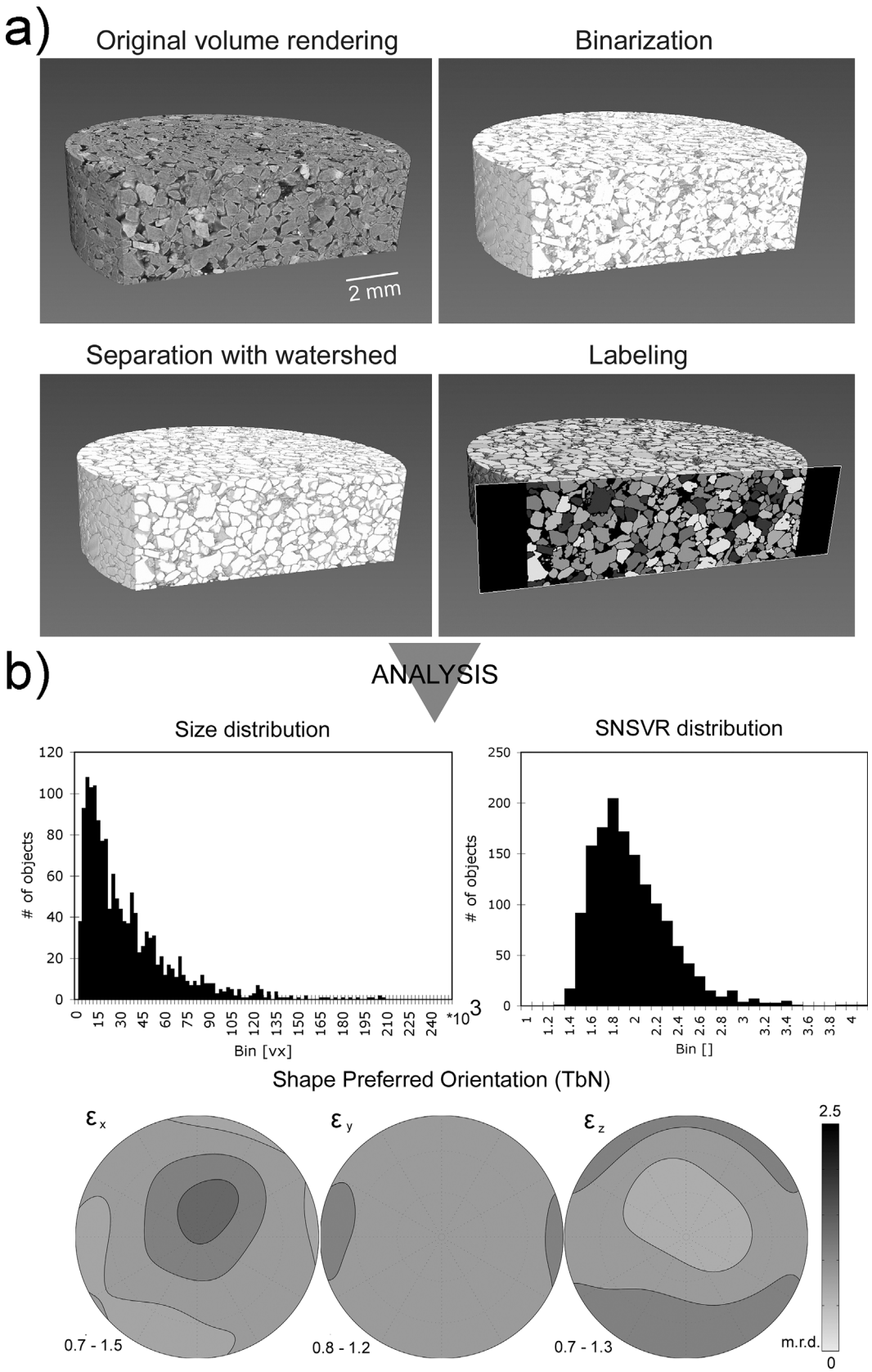

Fig. 4. Morphometric analysis of the sandstone sample: sequence of the essential basic operations for the data treatment (a) and examples of morphometric parameters obtained from the analysis of the rendered subvolume (b): see text for details. Pole figures represent the Texture by Number (TbN) approach on the analysis of the sand grains, and the scale is in multiples of random distribution (m.r.d.).

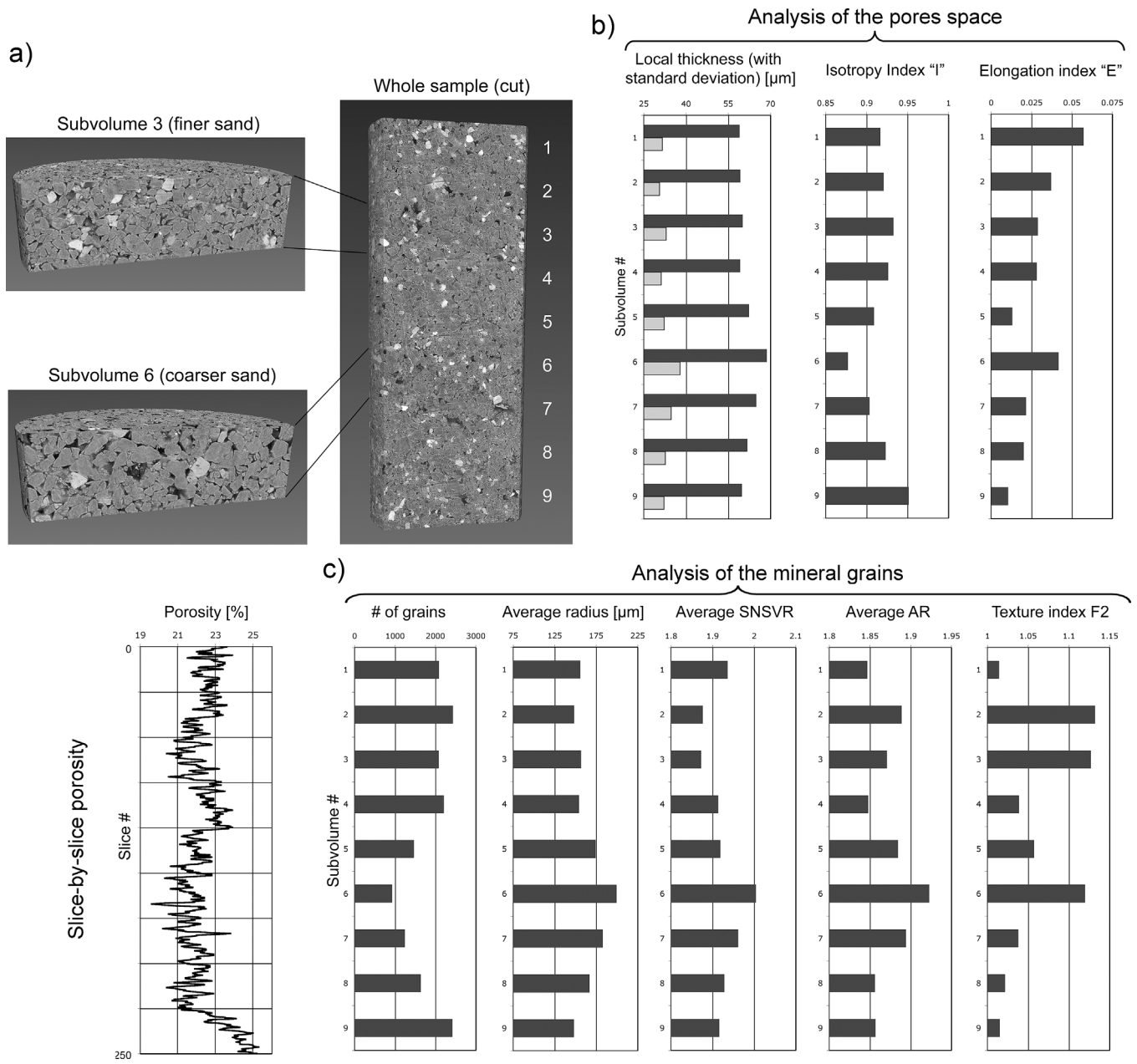

Fig. 5. Volume renderings of the sample (panel a) with associated morphometric analysis of the pore space (panel b) and sand grains (panel c) as a function of volume subsection.

visible in grain size and shape characteristics, likely generated during deposition. To better emphasize this feature in our sample, we performed an object size labeling on the binary dataset with the separated sand grains to obtain a volume where the gray value of each object is proportional to the volume of the object itself. Upon applying a different color table, to obtain a better visual contrast of the different grains, the result is shown in Fig. 6, where the volume rendering of the starting sample, panel (a), and the same labeled, volume, panel (b), are presented, both showing the same cut plane. Now the differences in grain size on the different locations in the sample are evident. Three zones with a slightly smaller sized grains are present (tiles 2, 4, and 9 in Fig. 5) as well as a 7 mm zone in the lower section of the sample with a larger mean grain size (tiles 5, 6, and 7 in Fig. 5). The differences are relatively small, ~55 µ in mean grain radius, but as will be seen in the subsequent sections, exert a dominant control on $scCO_2$ distribution.

3.3. Morphometric characteristics of pores

While the deposited frame consists of grains, the injection of $scCO_2$ is a process that occurs in the pore space, the morphometric analysis of the latter yields information about pores and throats, fundamental to flow dynamics. Unfortunately, the same approach used for the grains cannot be fully applied here. In interstitial structures, such as the pore space in granular materials, the separation of different pores is not a straightforward task. In fact, precisely defining the pore throats and the single pores in three dimensional datasets is problematic. To overcome this issue, we decided not to operate on a strictly object-based approach, where the separation of different objects (e.g. single pores) is required for the final analysis, when possible. The results are plotted in panel (b) of Fig. 5.

To obtain information about pores and throat sizes, a strategy borrowed from trabecular analysis in bones has been adopted, an approach referred to as local thickness calculation. The term "local thickness" is defined as the diameter of the largest sphere that fits inside

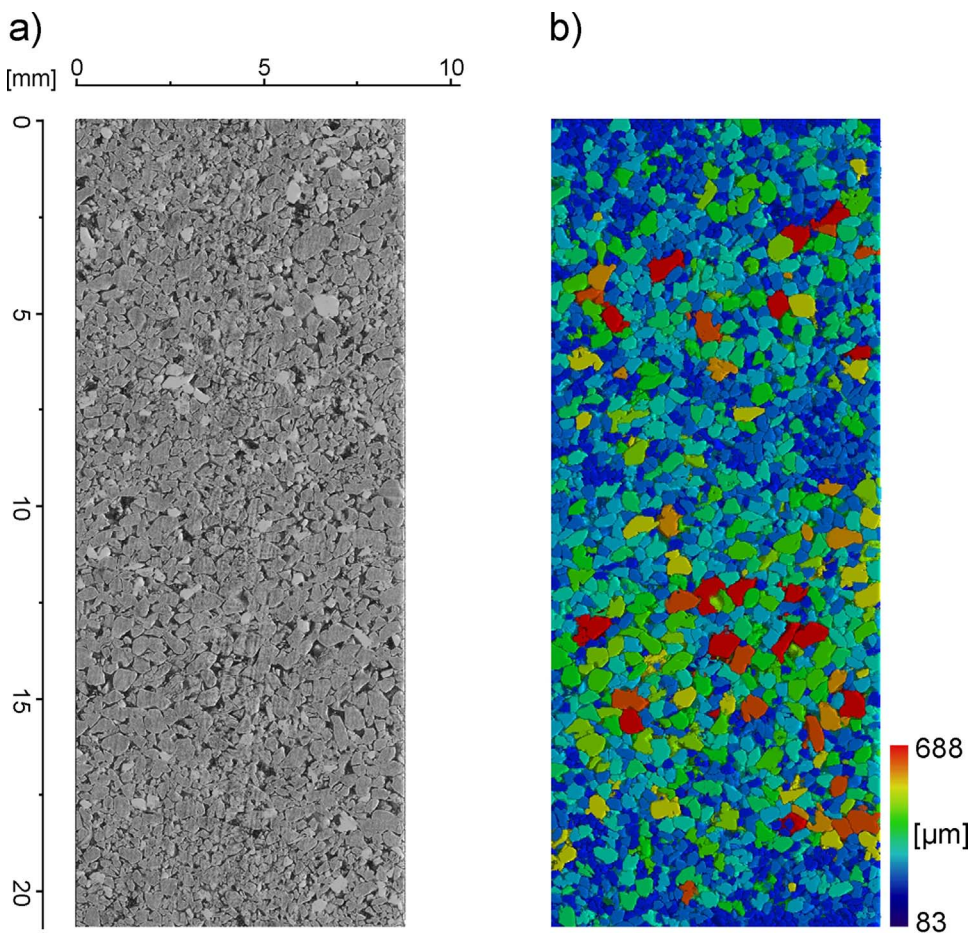

Fig. 6. Volume rendering of a vertical virtual cut of the sample. On the left the sand grains are rendered with their XR attenuation values, on the right the same sample shows the grains labeled with a color corresponding to their (equivalent volume sphere) diameter.

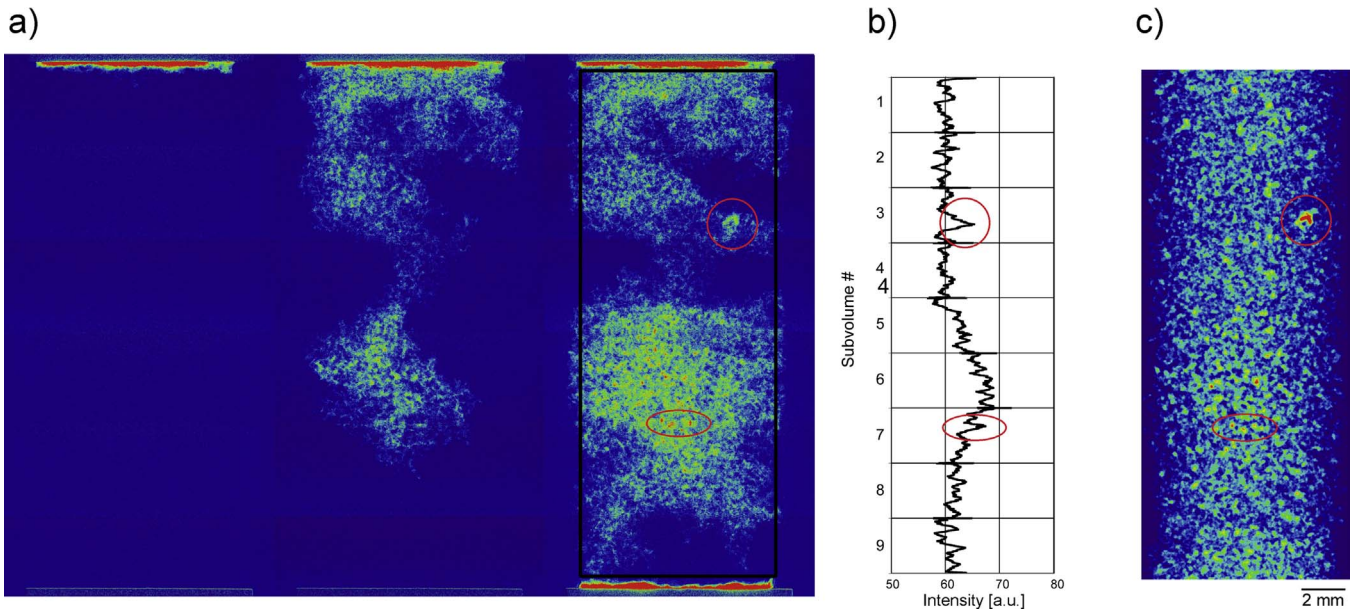

Fig. 7. Dynamic SXR radiography of the $scCO_2$ invasion process. Panel (a) shows a sequence of radiographs showing the invasion of the $scCO_2$ in the sample, with the rightmost radiograph in this panel being the sample at the final stage, measured in 3D and used for the simulations. Panel (b) shows a slice-by-slice local thickness value. Panel (c) depicts a local thickness average projection along the XR direction for comparison. Some of the shared features (bigger pores filled with $scCO_2$) in the different figures have been highlighted for clarity (red circles). (For interpretation of the references to colour in this figure legend, the reader is referred to the web version of this article.)

the object and contains the voxel, which implies the size of the pore body; "local thickness" calculations are equivalent to the Maximum Inscribed Sphere approach presented by Silin and Patzek (2006). The local thickness volume of the pore space has been calculated using a Fiji plugin (Dougherty and Kunzelmann, 2007) and the average values and standard deviations for the different subvolumes are plotted in Fig. 5. These data have also been used to obtain a slice-by-slice local thickness graph, where the variations within the sample are visible more in detail

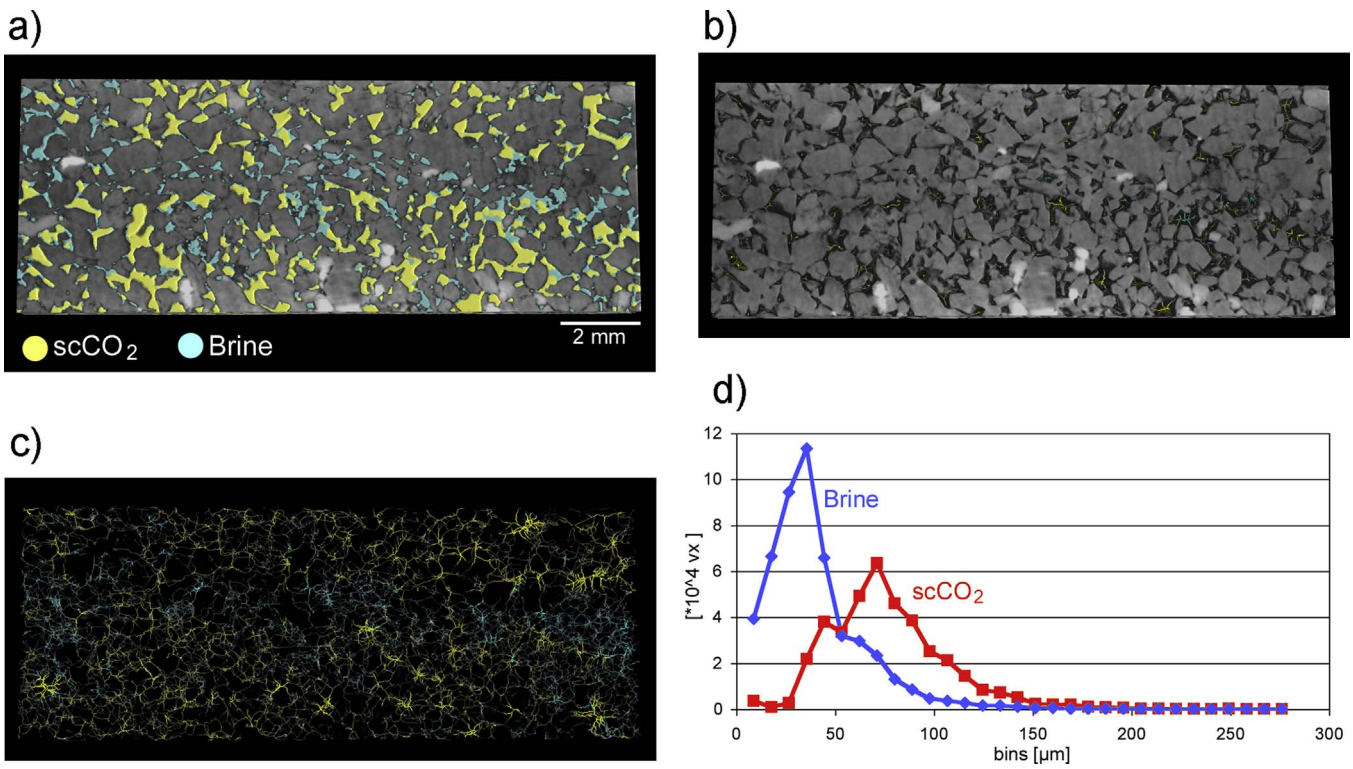

Fig. 8. SXR-µCT of a portion of the sample after the invasion process plus data analysis. In this figure, a virtual thin slab (chosen for clarity purposes) of the sample is shown. Panel (a) shows a volume rendering of the sand grains with the two fluids segmented (light blue = brine, yellow = $scCO_2$). Panel (b) depicts the X-ray gray scale with the thickness labeled skeleton (see text). Panel (c) shows the same thickness labeled skeleton without the grain overlay. Panel (d) depicts the pore occupancy histograms for $scCO_2$ and brine labeled components, demonstrating the affinity of $scCO_2$ to occupy the larger pores.

(Fig. 7, panels B & C). To quantify the anisotropy in the pore space, the well-known Mean Intercept Length (MIL) metric was chosen, since it does not require the separation of the objects (Harrigan and Mann, 1984). To quantify the fabric anisotropy present in the pores space, we used the isotropy (I) and elongation (E) indices (Fig. 5; Benn, 1994). The MIL analysis was performed with Quant3D (Ketcham, 2005b) using a spherical sub-sample and a uniform seeding grid.

Several observations can be made with respect to the morphological analysis of the pore space. First, the local thickness analysis shows that the zone with the largest mean grain size (tile 6) also has the largest mean local thickness, a metric for pore mean size (Fig. 5). More surprisingly, the same tile also has slightly lower porosity levels as shown by the slice-by-slice porosity analysis. From the results, it is possible to appreciate that the local anisotropy of this sample was very low (values very close to 1 for I, and close to 0 for E), in accordance with the findings in the sand grains shape preferred orientation analysis. In this case, any flow anisotropy is derived from the depositional laminations rather than sub-mm grain or pore preferred orientation.

4. Results: image analysis of µCT datasets of $scCO_2$ invasion

4.1. Radiographic analysis of $scCO_2$ invasion

Given the data acquisition time required to acquire a full tomographic dataset of the entire sample, the $scCO_2$ invasion process was monitored using tiled radiography. In the radiographic acquisition, only a single projection of the sample is recorded, compressing all sample variations into a single plane. Since our sample was considerably taller than the vertical beam extent, our radiographic acquisition involved vertical translation of the sample to acquire the same projection angle across the full length. The radiographs were then normalized, stitched, and differenced to yield a map of the drainage front during $scCO_2$ invasion. With filtered white beam acquisition, we were able to acquire tiled radiographs in less than a second, a temporal resolution that allowed monitoring the fast invasion process.

Fig. 7 presents a sequence of differential radiographs, where green-to-red colors indicate integrated density reduction (e.g. $scCO_2$ replacing brine) while blue colors indicate no change, showing the invasion process (inlet at the top), with 3 stages of the invasion process corresponding to before sample breakthrough (left in panel a), immediately after sample breakthrough (middle in panel a), and after the $scCO_2$ percolation to the outlet (right in panel a), which occurred in a span of approximately 3 min. The roughness of the sample ends yielded $scCO_2$ accumulation at the inlet and outlet contact. The slice-by-slice local thickness/porosity plot is also shown, as well as a weighted average image calculated along the X-ray direction from the pores space local thickness volume (in panel c). The last calculation effectively simulates a radiograph of the local thickness map and allows identification of features in common with the real radiograph showing the invasion of the $scCO_2$. In particular, the main focus is to evaluate if the $scCO_2$ preferentially invades the largest pores, such that a correlation between $scCO_2$ content and high average local thickness values would occur. A qualitative observation of the radiographs suggests that the local thickness and the $scCO_2$ invasion are related, as can be seen from highlighted features in Fig. 7, however, the local thickness alone (see simulated radiograph in Fig. 7C) cannot explain many features without taking into account fundamental constraints such as preferential flow paths.

4.2. Tomographic analysis of $scCO_2$ drainage – pore occupancy statistics

The availability of a tomographic dataset with the actual distributions of brine and $scCO_2$ allowed us to perform an in-depth analysis, particularly with regards to the relationship between 2-phase pore occupancy and pore morphology.

To investigate this relationship, we decided to perform a labeled

skeleton analysis; the skeleton of the pore space was calculated to obtain a topological description of the ideal pathways in the pores space. A simple medial-axis-retaining algorithm, the thinning algorithm, was chosen to calculate the skeleton, as implemented in the Skeletonize3D plugin in imageJ (Lee et al., 1994). The local thickness of the pore space was calculated using the procedure previously described for both the brine and $scCO_2$. The skeleton and the local thickness datasets were then merged to obtain a skeleton where the voxels have been labeled with the values of the local thickness, *and* the occupying fluid phase (see Fig. 8), allowing direct evaluation of the relationship between pore morphology and $scCO_2$ entrance. From this new skeleton, it was then straightforward to calculate local thickness frequency histograms for both the fluid phases (Fig. 8). This histogram shows very clearly how the two phases are distributed in relation with the local thickness in the pores space: the $scCO_2$ easily invades the largest pores, while the capillary forces in the smaller pores are strong enough to prevent the brine of being displaced by the $scCO_2$. The plotted histogram describes this process in a quantitative fashion. It is worth remarking that from the radiographs in Fig. 7, it is possible to appreciate how the residual brine is preferentially left in the layers where both the pores and sand grains are relatively small in size, highlighting a sub-mm bedding mentioned in our initial matrix analysis. A further analysis of the labeled skeleton can provide the size of the throats and their distribution. An intersection of the volume of the skeleton with the one with the watershed for the pore space can provide the distribution of the throats. Each throat can be assigned a size by labeling it with the local thickness volume values. Which phase is present in the throats can be obtained again by labeling with the brine and $scCO_2$ volumes. The resulting volumes provide information about both throat size and fluid occupancy, as visualized in the thin (for sake of clarity) subvolume, and plotted in the graph for the whole dataset in Fig. 9. Again it is possible to see that the brine occupies the smallest throats, while the largest ones are preferentially occupied by the $scCO_2$.

This analysis clearly illustrates that the variations in local thickness along the flow paths is the most important parameter related to the distribution of the invading $scCO_2$ in the sample. This information can be used as a starting point for the development of geometrical models that aim to predict the distribution of the invading $scCO_2$ in samples measured by μCT.

5. Results: a predictive model for drainage

5.1. Quantitative pore scale modeling of $scCO_2$ distribution

In this section, we present a simple model that effectively replicates the distribution of $scCO_2$ in the sample, based on the concept of local thickness and connectivity. We use an algorithm similar to Silin et al. (2010) to calculate the $scCO_2$ distribution during drainage. As with the original approach, the main assumptions in the method are that the pore space is i) fully saturated with two immiscible incompressible fluids, one perfectly wetting and one perfectly non-wetting, ii) the system is in thermodynamic equilibrium, iii) gravity is a negligible factor, iv) drainage occurs at low capillary numbers ($Ca < 10^{-6}$) where capillary forces are dominant, and v) dynamics are unimportant (quasi-static approximation). In these situations, the static interface between the two fluids can be described locally by the Young-Laplace equation,

$$p_c = 2\frac{s}{R} \tag{1}$$

where p_c denotes the capillary pressure, s, is the fluid–fluid interfacial tension coefficient, and R is the radius of curvature of the solid surface, e.g. a cylindrical pore radius. The general approach of the technique is to calculate a local R for every voxel within the pore space using the MIS approach and then generate a corresponding local capillary pressure associated with each voxel. The pore space is then subjected to an increasing fictitious pressure, p_i, and voxels are invaded according to the connected voxels which satisfy $p_c < p_i$. This process generates a sequence of invaded volumes during drainage, but is independent of generating a network representation or replicating the dynamics of the multiphase flow process. The boundary condition in this type of simulation is the location where the connected invasion/drainage process begins, in our case the injection surface of the sample. The procedure for this approach can be summarized in the following steps:

- Generating a binary volume of the pore space.
- Calculate the local thickness volume of the binary volume, generating a 32 bit volume with the voxels labeled with the different R values.
- Insert an inlet with 100% porosity above the 1st slice.
- For each i value from 1 to R_{MAX}, set a threshold of the 32 bit volume, generating a series of binary volumes.
- Calculate the components connected to the inlet, and remove it.
- Convert the $R_{(i)}$ to $p_{c(i)}$.

This procedure provides as the output a series of volumes simulating the invasion of $scCO_2$, as well as a curve relating inlet pressure to saturation during drainage. The entire approach is implemented as an ImageJ plugin and allows processing of a complete flood experiment on our whole sample dataset in less than 2 h on a modern desktop computer, highlighting the computational efficiency of the approach for large image volumes.

Fig. 10 shows the measured and the simulated radiographss of the $scCO_2$: as can be visually appreciated, the modeled distribution of the $scCO_2$ is very similar to the measured one. It is worth remarking how the layered structure is captured by the model as well as more localized features, such as larger pores filled with $scCO_2$. The differences present

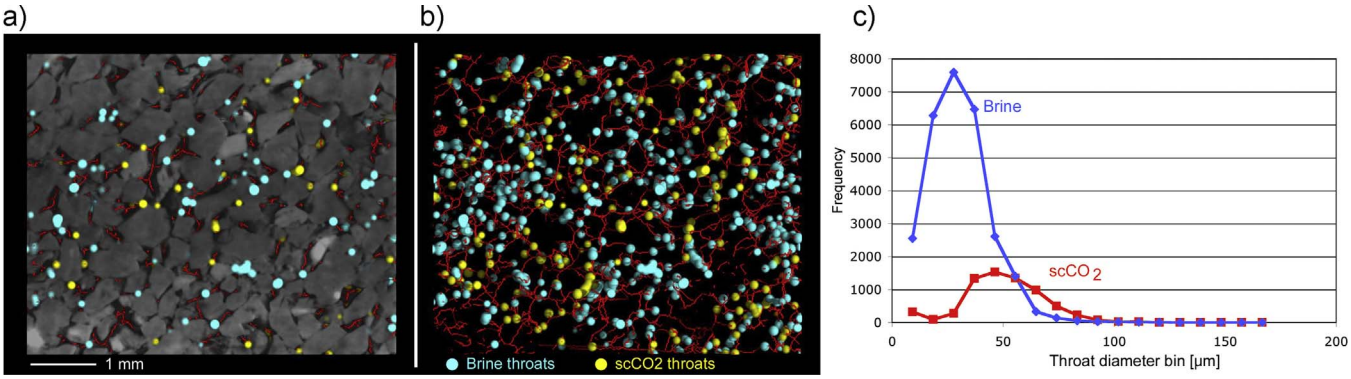

Fig. 9. Volume rendering of a subvolume showing the skeleton (red) and the throats (spheres colored with respect the fluid in that throat) with (panel a) and without (panel b) the grain overlay. Panel (c) depicts the throat occupancy histogram for the two fluid phases. (For interpretation of the references to colour in this figure legend, the reader is referred to the web version of this article.)

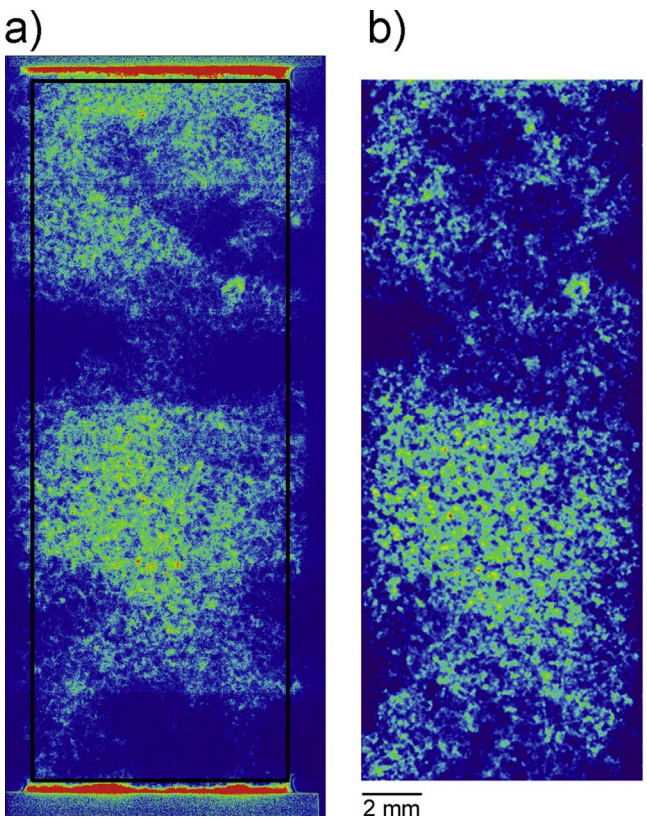

Fig. 10. Measured (left, a) and calculated (right, b) radiographs (displayed using a lookup table that highlights differences) of the $scCO_2$ invading the sample. The frame on the measured radiograph shows how the sample was cropped for the analysis.

in the two distributions are generally due to the boundary conditions: the modeled volume was cropped before the analysis to remove the outer layer of grains in the sample. This was required because of anomalous KI concentration in the very outer rim of the sample, in contact with the jacket. In the following example, utilizing the 3D volume, we demonstrate how the main sources of error in the modeled distribution of the $scCO_2$ are generally localized at the boundary part of the sample close to the outer surface.

As mentioned in the prior section, only a single subvolume of the sample was measured after $scCO_2$ invasion using μCT, because of a stepper motor failure during the experiment. While the radiograph-inferred distribution of the two phases seems to be reliable, we also directly compare the measured and calculated $scCO_2$ volumes in 3D. In Fig. 11 we show two vertical thin slices cut from the measured sample with the measured volume in panel A and the simulated volume in panel B. The volume rendering of the grains (gray) is shown, along with both the measured and calculated distributions of the fluids. It is possible to appreciate immediately that the brine (light blue) and the $scCO_2$ (yellow) are accurately replicated by the simulation (panel B), with the main errors being some small ganglia connected to the outer part of the sample, suggesting that this issue is due to the non perfect boundary conditions due to the cropping. The resemblance of the two distributions is strikingly similar, especially when considering the simplicity of the approach used to model the invaded volume.

In Fig. 12, an even small sub-volume from the larger section is considered to allow pore-scale evaluation; in this case, it is possible to appreciate how the simulation (Fig. 12, panel B) satisfactorily predicts the distribution of the $scCO_2$ also at the scale of single pores. It can be seen that the center of larger pores is invaded by the non-wetting fluid while brine continues to occupy thinner inter-granular contacts, throats, and smaller pores where a higher capillary pressure would be required for the displacement of the wetting fluid (see e.g. the details in highlighted by the red circles). Places where the simulation has difficulty include brine film thickness estimation; modeled results generate a larger estimated film thickness. In aggregate however, the MIS-based model predicts bulk saturations within 4–7% of the measured values when compared on a slice-by-slice basis.

5.2. Prediction of pressure-Saturation curves

Using the obtained SXR-μCT dataset of the pore structures, it was also possible to go a step further and estimate a capillary pressure-saturation curve for Hg porosimetry. In this comparison, we used one half of the sample volume obtained from the tomographic experiment to calculate the pressure-saturation curve. Then, we measured the pressure-saturation curves on the same half of the sample with a Hg pycnometer. The calculated (for both the halves of the sample, to check consistency) and measured pressure-saturation curves for the Domengine sandstone sample are plotted in Fig. 13. The raw data of the measured curve have been treated accordingly to the method proposed in Pini and Benson (2013) to calculate the first entry pressure for the sample.

Several issues needed to be taken into account for this modeling part: the sample was cut in half and put into the porosimeter with the jacket still covering the lateral surface of the cylinder, since it was not possible to take the jacket off without breaking the sample. Because of this problem, the inlets for Hg in the model were set as the two bases of the cylinder. The jacket was subject to weathering during the experiment: a significant number of small cracks developed in the jacket, which embrittled during the X-ray imaging measurement, such that a secondary jacket porosity was created. This porosity cannot be taken into account by the model, but of course impacts the Hg porosimeter curves. This is one of the reasons why the maximum porosity of the model is lower than the measured one. The modeled porosity is expected to be lower even in absence of such issues, as it cannot account for the porosity of the sample below the resolution of the SXR-μCT dataset, which in this sample has been further increased by the fine cracks in the jacket.

With these issues in mind, and considering the corrections listed above, the modeling of the Hg intrusion curve is consistent with the measured one as can be seen in Fig. 13. The two modeled halves of the sample (circles) are comparable, as should be expected due to the relatively low degree of sample heterogeneity, and the measured (solid diamonds) half of the sample overlap the calculated curved for the same volume (solid circles).

6. Discussion

6.1. Consistency of observed scCO2 drainage with prior studies

In our drainage experiment, the experiment was conducted at capillary numbers similar to past studies, all within the invasion/percolation regime, e.g. $Ca = 9 \times 10^{-7}$ in the case of Andrew et al. (2014), $Ca = 1 \times 10^{-8.6}$ in the case of Herring et al. (2014), and $Ca = 1 \times 10^{-6}$ for Iglauer et al. (2011). While many of these past experiments have focused on cluster analysis of the residually trapped phase (Andrew et al., 2013, 2014a), a few have explored the drainage phase in more detail (Iglauer et al., 2011; Herring et al., 2014). We measured initial $scCO_2$ saturations of ~58.9% in the Domengine sandstone after the drainage phase, slightly higher than the μCT measurements from Iglauer et al. (2011) of ~48% on the Doddington sandstone and lower than the measurements of Herring et al. (2014) of 91%, where their value is likely due to the presence of a hydrophilic membrane which was not used in our study. More generally, our experiment was entirely consistent with $scCO_2$ being the non-wetting phase at early stages of drainage, an observation in concurrence with prior studies.

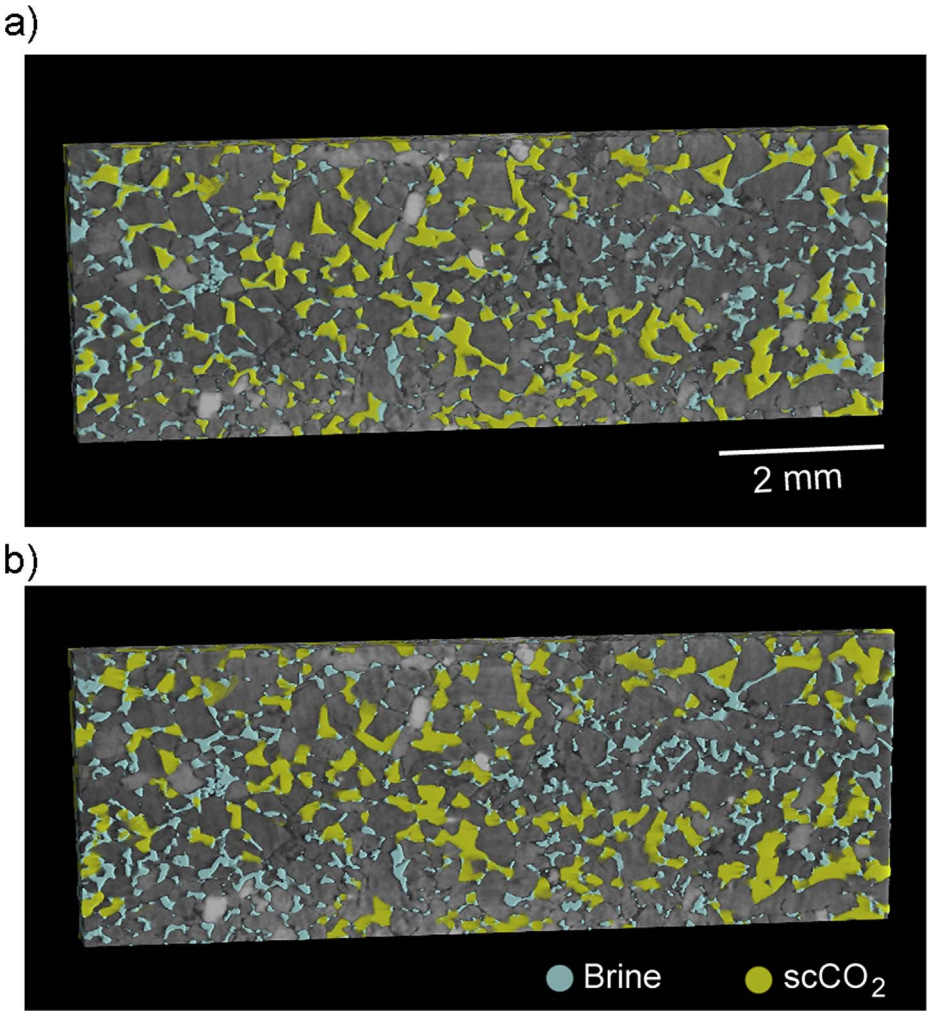

Fig. 11. Volume rendering of a subvolume (vertical thin section) showing the distribution of brine and $scCO_2$ in the measured (a, top) and simulated (b, bottom) datasets. It is possible to notice how the brine is not replaced by the $scCO_2$ in the smallest pores, this is particularly evident in the layer of finer sand in the center of the subvolume.

6.2. Role of micro-structural features

One unique aspect of our experiment is the selection of a sandstone formation with evidence of depositional structure and sorting variation. Past studies have selected samples with an exceptional degree of homogeneity such as the Bentheimer sandstone (e.g. Andrew et al., 2013; Herring et al., 2014) and the Ketton limestone (e.g. Andrew et al., 2013) to simplify analysis. In contrast, most GCS reservoir units are highly heterogeneous with depositional features evident in core. Nakagawa et al. (2013) provides an excellent example contrasting the $scCO_2$ distribution in a homogeneous Berea sample with that of a sample from the Tuscaloosa D unit, a reservoir rock from the SECARB Cranfield GCS pilot. Although the observations of Nakagawa et al. (2013) were at the mm scale (medical CT) and well above pore dimensions, thin laminations were the most obvious control on $scCO_2$ distribution and significantly impacted CO_2-induced seismic response.

In our study, we observed the important role of capillary barriers formed by sorting effects; layer 4 in our sample (see Fig. 5) exhibits slightly lower mean grain radii in comparison to adjoining sections, resulting in lower local thickness values (panel 5(b)). As a result, $scCO_2$ largely bypasses this layer after finding a single chain of larger pores, as can be seen in panel (a), Fig. 7. Even at the micron scale, thin

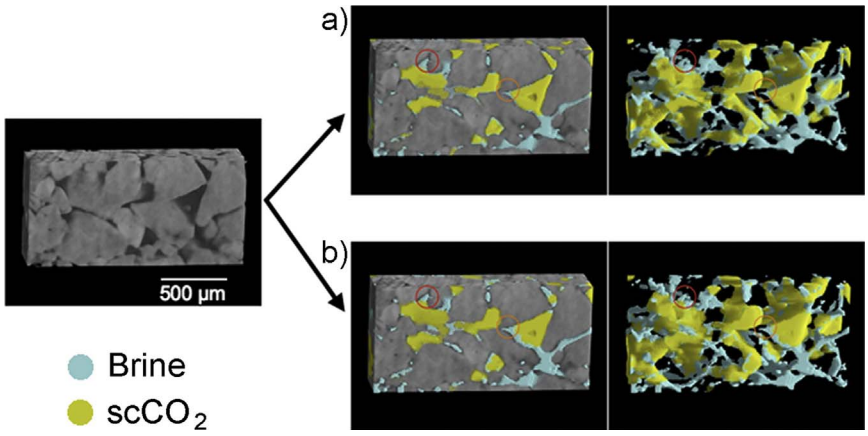

Fig. 12. Detail of the distribution of the two fluids in the pore space in a smaller subvolume, both in the measured (a, top) and simulated (b, bottom) datasets. The red circles highlight two fine structures that have been properly reproduced. (For interpretation of the references to colour in this figure legend, the reader is referred to the web version of this article.)

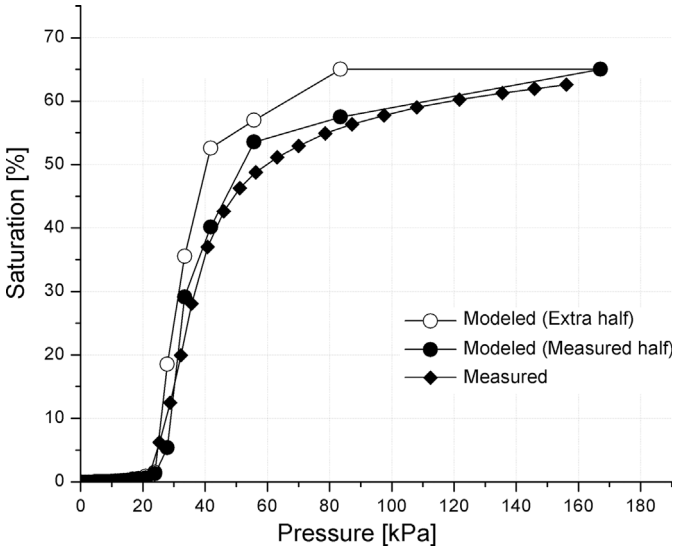

Fig. 13. Measured (diamonds) and calculated (circles) Pressure-Saturation curves for Hg porosimetry of the sandstone samples: the modeled half (solid circles) nicely overlaps to the Hg porosimetry measurement. The modeling on the other half of the sample gives slightly different results, but it still significantly similar to the measured curve.

laminations of only 2–3 grains of thickness, can play a role in fluid distribution as is seen in Fig. 8, panel (a), where a central layer of slightly smaller grains retains water during drainage. As a result of these effects, a strong depositional fingerprint exists on the macroscopic $scCO_2$ distribution, a phenomenon already observed at the larger scale. As shown in Fig. 11, our modeling approach captures the appropriate physics to replicate these effects when pore-scale geometry is available.

Our results suggest that studies investigating micron to m scale CO_2 geometries in a field setting would benefit from careful sedimentological mapping to identify small features which may exert control of flow during the drainage process. Our observations also validate larger scale modeling studies that rely on invasion percolation (IP) simulations to predict flow at the mesoscale (cm to m);

Meckel (2013) and Ganesh et al. (2013) present such a methodology utilizing topographical measurements of sedimentary-relief peels with resolution on the mm scale, equivalent to the small laminations seen in our datasets. In a GCS environment, similar data with excellent vertical but sparser lateral support might be derived from borehole imaging approaches e.g. Formation Micro-Imager (FMI) datasets.

6.3. Comments on forward modeling limitations

As shown in Figs. 10–12, our IP-MIS modeling algorithm, a variant of the approach presented by Silin et al. (2011), proved quite effective in capturing the core-to-pore scale $scCO_2$ distribution in this particular sample. The small differences observed demonstrated limitations of the approach including the sensitivity of the simulation to domain boundaries, both inlet zones and near-jacket features. In the radiography comparison (Fig. 10), jacket boundary features contributed to observation/simulation mismatch while in the CT comparison (Fig. 11), the lack of a measured inlet boundary proved important. Based on these observations, we emphasize the need to capture high quality imagery of the entire sample including domain boundaries if quantitative pore scale comparisons of 2-phase flow are desired.

At the pore scale, while deviations appear small, they are typically most obvious at pore boundaries where the simulation over-estimates brine film thickness and occasionally predicts brine occupancy where $scCO_2$ is observed. This could be due to the presence of surfaces which are not strongly water wet (mixed wet), due to either existing organic residue or modification due to $scCO_2$ exposure. The topology of the system and the nature of the surfaces likely have some effects as well (Liu et al., 2017). While the pore and throat occupancy histograms shown in Figs. 8 and 9 demonstrate the system is largely water wet, individual pores could have different properties. Recent work by Tokunaga et al., (2013) and Wang and Tokunaga (2015) suggest that $scCO_2$ exposure can drive dewetting in both quartz and carbonate systems; while we do not see the aggregate behavior described in those studies, our short exposure experiments could have selectively altered a small number of surfaces, thus breaking the simulation assumptions of entirely water-wet grain surfaces, a scenario that seems unlikely but we cannot exclude.

6.4. Areas of application for CO_2 distribution maps

While the approach we validate for $scCO_2$ distribution modeling is limited to the drainage phase at present, such a distribution is of significant value in a variety of secondary calculations required for scaling up to continuum property estimation. The first and perhaps most obvious example is that of calculating relative permeability curves for the drainage leg, demonstrated by Silin and Patzek (2009) and more recently by Hussain et al. (2014), Berg et al. (2016), and Zuo et al. (2016) for exsolution. In these approaches, an inexpensive estimate of the $scCO_2$ phase distribution can be used to estimate brine permeability at each step by treating the $scCO_2$ as immobile and modeling Stokes flow through the brine-occupied pore space. A similar approach can be used to estimate effective diffusivity during partial saturation states by calculating diffusivity numerically at each saturation step.

Another important estimation problem during the drainage phase is $scCO_2$ dissolution into brine at early times. The kinetics of CO_2 dissolution is constrained by, among several parameters, the brine/$scCO_2$ surface area, a value which can be calculated as a function of saturation using the simulation results described in this study. This interfacial area term is typically calculated for spherical bubbles (e.g. Holocher et al., 2003) to solve the mass transfer problem in a simple form.

A final and promising problem for which pore-scale CO_2 distribution maps might be applied is that of seismic property estimation. As mentioned previously, one significant use of our validated model for pore-scale drainage estimation is calculation of $scCO_2$ distribution to estimate “patch” sizes (e.g. White 1975), required for inversion of the seismic response in GCS monitoring. While a small number of studies have estimated $scCO_2$ seismic patch sizes in the field (e.g. Caspari et al., 2011) or laboratory (Nakagawa et al., 2011), pore-scale imaging and modeling offer another approach to directly estimate patch dimensions, or to model seismic response directly.

6.5. Advantages of phase retrieval

From a technical perspective, we have also shown that the application of advanced reconstruction procedures from the projections obtained from the SXR-μCT experiment can provide much better quality data than the ones obtained with the conventional filtered back-projection applied directly to the radiographs. In particular, the phase-retrieval approach we have utilized, while originally developed for monochromatic X-rays and phase objects, has proven effective even for absorbing samples collected using hardened synchrotron white light (Weitkamp et al., 2001). This technique is still not broadly used in geosciences and circumvents challenging segmentation problems in 3-phase systems exacerbated by phase contrast artifacts. With the availability of user-friendly packages and high performance implementations (e.g. ANKAphase: Weitkamp et al., 2011; PITRE: Chen et al., 2012; TomoPy, Gürsoy et al., 2014; STP, Brun et al., (2017), etc.), this approach will likely see a broader application in the geosciences in the near future (see e.g. Arzilli et al., 2015, 2016; Zambrano et al., 2017).

6.6. Steps towards imbibition observations and modeling

While we present results collected during the drainage phase, an

improved suite of observational datasets and modeling tools for imbibition are clearly desired; such tools would provide greater insight of the $scCO_2$ residual trapping process, a challenging target for direct simulation. From an experimental point of view this presents some additional challenges such as the requirement of having a system stable for a longer time, and a slightly more complicated experimental setup; recent studies including Andrew et al. (2014a,b) and Herring et al., (2016) have achieved this goal. Hardware improvements, particularly in the field of 2D X-ray detectors, are allowing collection of complete tomographic datasets much faster than in the recent past, allowing to follow *in situ* fast processes such e.g. Haines jumps (Berg et al., 2013), magma vesiculation (Baker et al., 2012), etc. where a full dataset can be acquired in the range of few seconds. These new capabilities could be used to better monitor the drainage and imbibition processes with finer temporal resolution, allowing the study of droplet dynamics. From a modeling point of view, the MIS/IP approach we have adopted for drainage simulation cannot be utilized for imbibition. While a variety of network models exist for the imibition process (e.g. Blunt et al., 2013), they typically require significant calibration due to geometric pore-throat approximations; rapid advances in direct modeling using lattice-Boltzman methods (e.g. Jiang and Tsuji, 2016) and related direct solution techniques may provide an avenue forward. Other factors influencing the distribution and the stability of the $scCO_2$ ganglia need further studies as well, from both the experimental and modeling points of view. Such additional factors that can occur include, phenomena such as gravity driven migration (buoyancy), chemical diffusion driven migration (e.g. Ostwald ripening), dissolution, mineralization, and wettability alteration (e.g. Kim et al., 2012; Tokunaga et al., 2013; Wang and Tokunaga, 2015). Unfortunately the time frame of some of these processes often conflicts with the experimental requirements, that commonly cannot be pushed longer than a few days, therefore the modeling approach, supported by short-term experimental observations, becomes a necessity.

7. Conclusions

In the present work, we have shown a complete approach for the visualization and simulation of $scCO_2$ drainage (invasion) in a reservoir sandstone at *in situ* conditions; this includes experimental utilization of a high-pressure triaxial cell suitable for synchrotron X-ray μCT, a comprehensive morphological analysis approach, and a simple quasi-static predictive model of the drainage process. For each of these steps, technical advances have been demonstrated including novel experimental and data reduction steps. In the data analysis stage, we have employed advanced morphometric analysis techniques to quantify the microstructural characteristics of the sample and find which parameters are the ones important to understand the drainage process. With those results, a simplified quasi-static drainage model was implemented and shown to accurately replicate the experimental observations of $scCO_2$ distribution at the pore scale without secondary calibration datasets, thus providing a validated predictive tool, now requiring only a dry tomographic scan for simulation. The same modeling approach is capable of replicating Hg MICP data, increasing our confidence in the algorithm. The described study provides an observational and modeling framework for future efforts requiring access to pore scale $scCO_2$ distribution for prediction of macroscopic hydrological or chemical properties relevant to geological carbon storage.

Acknowledgments

This work was supported as part of the Center for Nanoscale Control of Geologic CO_2 (NCGC), an Energy Frontier Research Center funded by the U.S. Department of Energy, Office of Science, Basic Energy Sciences under Award # DE-AC02-05CH11231. The SXR-μCT experiments were performed with the assistance of Alastair MacDowell and Dula Parkinson at the Advanced Light Source, Beamline 8.3.2, supported by the U.S. DOE Office of Science, Office of Basic Energy Sciences (DE-AC02-05CH11231). The Domengine sandstone samples were kindly provided by Dr. Tim Kneafsey, collected with the permission of Black Diamond Regional Preserve, administered by the East Bay Regional Parks District. Gautier Landrot and Brian Bonner are also acknowledged for the help during the SXR-μCT measurements.

References

Øren, P.E., Bakke, S., 2003. Reconstruction of Berea sandstone and pore-scale modelling of wettability effects. J. Petrol. Sci. Eng. 39 (3), 177–199.
Ajo-Franklin, J.B., Peterson, J., Doetsch, J., Daley, T.M., 2013. High-resolution characterization of a CO_2 plume using crosswell seismic tomography: cranfield, MS, USA. Int. J. Greenh. Gas Control 18, 497–509.
Andrew, M., Bijeljic, B., Blunt, M.J., 2013. Pore-scale imaging of geological carbon dioxide storage under in situ conditions. Geophys. Res. Lett. 40 (15), 3915–3918.
Andrew, M., Bijeljic, B., Blunt, M., 2014a. Pore-scale imaging of trapped supercritical carbon dioxide in sandstones and carbonates. Int. J. Greenh. Gas Control 22, 1–14.
Andrew, M., Bijeljic, B., Blunt, M.J., 2014b. Pore-by-pore capillary pressure measurements using X-ray microtomography at reservoir conditions: curvature, snap-off, and remobilization of residual CO_2. Water Resour. Res. 50 (11), 8760–8774.
Andrew, M., Menke, H., Blunt, M.J., Bijeljic, B., 2015. The imaging of dynamic multiphase fluid flow using synchrotron-based X-ray microtomography at reservoir conditions. Transp. Porous Media 110 (1), 1–24.
Armstrong, R., Ajo-Franklin, J., 2011. Investigating biomineralization using synchrotron based X-ray computed microtomography. Geophys. Res. Lett. 38 (8).
Arzilli, F., Mancini, L., Voltolini, M., Cicconi, M.R., Mohammadi, S., Giuli, G., Mainprice, D., Paris, E., Barou, F., Carroll, M.R., 2015. Near-liquidus growth of feldspar spherulites in trachytic melts: 3D morphologies and implications in crystallization mechanisms. Lithos 216, 93–105.
Arzilli, F., Polacci, M., Landi, P., Giordano, D., Baker, D.R., Mancini, L., 2016. A novel protocol for resolving feldspar crystals in synchrotron X-ray microtomographic images of crystallized natural magmas and synthetic analogs. Am. Mineral. 101 (10), 2301–2311.
Baker, D.R., Brun, F., O'Shaughnessy, C., Mancini, L., Fife, J.L., Rivers, M., 2012. A four-dimensional X-ray tomographic microscopy study of bubble growth in basaltic foam. Nat. Commun. 3, 1135.
Bakke, S., Øren, P.E., 1997. 3-D pore-scale modelling of sandstones and flow simulations in the pore networks. SPE J. 2 (02), 136–149.
Benn, D.I., 1994. Fabric shape and the interpretation of sedimentary data. J. Sediment. Res. A64, 910–915.
Berg, S., Ott, H., Klapp, S.A., Schwing, A., Neiteler, R., Brussee, N., Makurat, A., Leu, L., Enzmann, F., Schwarz, J.O., Kersten, M., 2013. Real-time 3D imaging of Haines jumps in porous media flow. Proc. Natl. Acad. Sci. 110 (10), 3755–3759.
Berg, S., Rücker, M., Ott, H., Georgiadis, A., van der Linde, H., Enzmann, F., Kersten, M., Armstrong, R.T., de With, S., Becker, J., Wiegmann, A., 2016. Connected pathway relative permeability from pore-scale imaging of imbibition. Adv. Water Resour. 90, 24–35.
Blunt, M., King, P., 1991. Relative permeabilities from two-and three-dimensional pore-scale network modelling. Transp. Porous Media 6 (4), 407–433.
Blunt, M.J., Bijeljic, B., Dong, H., Gharbi, O., Iglauer, S., Mostaghimi, P., Paluszny, A., Pentland, C., 2013. Pore-scale imaging and modelling. Adv. Water Resour. 51, 197–216.
Borgefors, G., 1996. On digital distance transforms in three dimensions. Comput. Vision Image Understand. 64 (3), 368–376.
Bronnikov, A., 2002. Theory of quantitative phase-contrast computed tomography. J. Opt. Soc. Am. 19 (3), 472–480.
Brun, F., Massimi, L., Fratini, M., Dreossi, D., Billé, F., Accardo, A., Pugliese, R., Cedola, A., 2017. SYRMEP Tomo Project: a graphical user interface for customizing CT reconstruction workflows. Adv. Struct. Chem. Imaging 3, 4.
Bryant, S., Blunt, M., 1992. Prediction of relative permeability in simple porous media. Phys. Rev. A 46(4 (2004).
Bunge, H.J., 1982. Texture Analysis in Materials Science: Mathematical Methods. P.R. Morris Trans, Butterworths, London.
Caspari, E., Muller, T.M., Gurevich, B., 2011. Time-lapse sonic logs reveal patchy CO_2 saturation in-situ. Geophys. Res. Lett. 38, L13301.
Chalbaud, C., Robin, M., Lombard, J.M., Martin, F., Egermann, P., Bertin, H., 2009. Interfacial tension measurements and wettability evaluation for geological CO_2 storage. Adv. Water Resour. 32 (1), 98–109.
Chen, R.-C., Dreossi, D., Mancini, L., Menk, R., Rigon, L., Xiao, T.-Q., Longo, R., 2012. PITRE: software for phase-sensitive X-ray image processing and tomography reconstruction. J. Synchrotron Radiat. 19, 836–845.
Cherven, V., 1983. Stratigraphy, facies, and depositional provinces of the middle eocene domengine formation, southern sacramento basin, workshop on cenozoic marine sedimentaion, pacific margin, USA. Pacific Section, Soc. Sedim. Geol.
Cinar, Y., Riaz, A., Tchelepi, H.A., 2007. Experimental study of CO2 injection into saline formations. SPE Annual Technical Conference and Exhibition. Society of Petroleum Engineers (2007, January).
Dierick, M., Masschaele, B., Van Hoorebecke, L., 2004. Octopus, a fast and user-friendly tomographic reconstruction package developed in LabView®. Meas. Sci. Technol. 15, 1366–1370.
Dougherty, R., Kunzelmann, K., 2007. Computing local thickness of 3D structures with ImageJ. Microsc. Microanal. 13, 1678–1679.

Gürsoy, D., De Carlo, F., Xiao, X., Jacobsen, C., 2014. TomoPy: a framework for the analysis of synchrotron tomographic data. J. Synchrotron Radiat. 21 (5), 1188–1193.
Ganesh, P.R., Bryant, S.L., Meckel, T.A., 2013. Characterizing small-scale migration behavior of sequestered CO2 in a realistic geologic fabric. Energy Procedia 37, 5258–5266.
Harrigan, T.P., Mann, R.W., 1984. Characterization of microstructural anisotropy in orthopedic materials using a second rank tensor. J. Mater. Sci. 19, 761–767.
Herring, A.L., Andersson, L., Newell, D.L., Carey, J.W., Wildenschild, D., 2014. Pore-scale observations of supercritical CO_2 drainage in Bentheimer sandstone by synchrotron x-ray imaging. Int. J. Greenh. Gas Control 25, 93–101.
Herring, A.L., Andersson, L., Wildenschild, D., 2016. Enhancing residual trapping of supercritical CO_2 via cyclic injections. Geophys. Res. Lett. 43. http://dx.doi.org/10.1002/2016GL070304.
Holocher, J., Peeters, F., Aeschbach-Hertig, W., Kinzelbach, W., Kipfer, R., 2003. Kinetic model of gas bubble dissolution in groundwater and its implications for the dissolved gas composition. Environ. Sci. Technol. 37 (7), 1337–1343.
Hu, Q., Quian, G., Nowinski, W.L., 2005. Fast connected-component labelling in three-dimensional binary images based on iterative recursion. Comput. Vision Image Understanding 99 (3), 414–434.
Hussain, F., Pinczewski, W.V., Cinar, Y., Arns, J.Y., Arns, C.H., Turner, M.L., 2014. Computation of relative permeability from imaged fluid distributions at the pore scale. Transport Porous Media 104 (1), 91–107.
IPCC, 2005. Special report on carbon dioxide capture and storage. In: Metz, O., de Coninck, H.C., Loos, M., Meyer, L.A. (Eds.), Prepared by Working Group III of the Intergovernmental Panel on Climate Change. Cambridge University Press, Cambridge, UK.
Iglauer, S., Paluszny, A., Pentland, C.H., Blunt, M.J., 2011. Residual CO_2 imaged with X-ray micro-tomography. Geophys. Res. Lett. 38 (21).
Jiang, F., Tsuji, T., 2016. Numerical investigations on the effect of initial state CO2 topology on capillary trapping efficiency. Int. J. Greenh. Gas Control 49, 179–191.
Kak, C., Slaney, M., 1987. Principles of Computerized Tomographic Imaging. IEEE Press, New York.
Ketcham, R.A., 2005a. Computational methods for quantitative analysis of three-dimensional features in geological specimens. Geosphere 1, 32–41.
Ketcham, R.A., 2005b. Three-dimensional grain fabric measurements using high- resolution X-ray computed tomography. J. Struct. Geol. 27 (7), 1217–1228.
Kim, Y., Wan, J., Kneafsey, T.J., Tokunaga, T.K., 2012. Dewetting of silica surfaces upon reactions with supercritical CO2 and brine: pore-scale studies in micromodels. Environ. Sci. Technol. 46 (7), 4228–4235.
Kneafsey, T.J., Silin, D., Ajo-Franklin, J.B., 2013. Supercritical CO_2 flow through a layered silica sand/calcite sand system: experiment and modified maximal inscribed spheres analysis. Int. J. Greenh. Gas Control 14, 141–150.
Landrot, G., Ajo-Franklin, J.B., Yang, L., Cabrini, S., Steefel, C.I., 2012. Measurement of accessible reactive surface area in a sandstone, with application to CO_2 mineralization. Chem. Geol. 318, 113–125.
Lee, T.C., Kashyap, R.L., Chu, C.N., 1994. Building skeleton models via 3-D medial surface axis thinning algorithms. CVGIP: Graph. Models Image Process. 56 (6), 462–478.
Liu, Z., Herring, A., Arns, C., Berg, S., Armstrong, R.T., 2017. Pore-scale characterization of two-phase flow using integral geometry. Transp. Porous Media 118 (1), 99–117.
MacDowell, A.A., Parkinson, D.Y., Haboub, A., Schaible, E., Nasiatka, J.R., Yee, C.A., Jameson, J.R., Ajo-Franklin, J.B., Brodersen, C.R., McElrone, A.J., 2012. X-ray micro-tomography at the advanced light source. SPIE Optical Engineering + Applications. International Society for Optics and Photonics, pp. 850618 (2012, October).
Meakin, P., Tartakovsky, A.M., 2009. Modeling and simulation of pore-scale multiphase fluid flow and reactive transport in fractured and porous media. Rev. Geophys. 47 (3).
Meckel, T.A., 2013. Digital rednering of sedimentary-relief peels: implications for clastic facies characterization and fluid flow. J. Sediment. Res. 83, 201–495.
Meyer, F., 1994. Topographic distance and watershed lines. Signal Process. 38, 113–125.
Meyers, G.R., Mayo, S.C., Gureyev, T.E., Paganin, T.M., Wilkins, S.W., 2007. Polychromatic cone-beam phase-contrast tomography. Phys. Rev. A 76, 045804.
Muskat, M., Meres, M.W., 1936. The flow of heterogeneous fluids through porous media. J. Appl. Phys. 7 (9), 346–363.
Nakagawa, S., Kneafsey, T.J., Daley, T.M., Freifeld, B.M., Rees, E.V., 2011. Laboratory seismic monitoring of supercritical CO2 flooding in sandstone cores using the Split Hopkinson Resonant Bar technique with concurrent X-ray CT imaging. In: 1st International Workshop on Rock Physics. August 7-12 2011 Golden, CO.
Nakagawa, S., Kneafsey, T.J., Daley, T.M., Freifeld, B.M., Rees, E.V., 2013. Laboratory seismic monitoring of supercritical CO_2 flooding in sandstone cores using the Split Hopkinson Resonant Bar technique with concurrent x-ray Computed Tomography imaging. Geophys. Prospect. 61 (2), 254–269.
Noiriel, C., Steefel, C.I., Yang, L., Ajo-Franklin, J., 2012. Upscaling calcium carbonate precipitation rates from pore to continuum scale. Chem. Geol. 318, 60–74.
Otsu, N., 1979. A threshold selection method from gray-level histograms. IEEE Trans. Syst. Man Cybern. 9, 62–66.
Paganin, D., Mayo, S.G., Gureyev, T.E., Miller, P.R., Wilkins, S.W., 2002. Simoultaneous phase and amplitude extraction from a single defocused image of a homogeneous object. J. Microsc. 206 (1), 33–40.
Patzek, T.W., 2000. Verification of a complete pore network simulator of drainage and imbibition. SPE/DOE Improved Oil Recovery Symposium. Society of Petroleum Engineers.
Pini, R., Benson, S.M., 2013. Simultaneous determination of capillary pressure and relative permeability curves from core-flooding experiments with various fluid pairs. Water Resour. Res. 49 (6), 3516–3530.
Ridler, T.W., Calvard, S., 1978. Picture thresholding using an iterative selection method. IEEE Trans. Syst. Man Cybern. 8, 630–632.
Roerdink, J.B.T.M., Meijster, A., 2001. The watershed transform: definitions, algorithms, and parallelization strategies. Fundam. Inf. 41, 187–228.
Rubino, J.G., Velis, D.R., Sacchi, M.D., 2011. Numerical analysis of wave-induced flow effects on seismic data: application to monitoring of CO_2 storage at the Sleipner field. J. Geophys. Res. 116, B03306.
Schindelin, J., Arganda-Carreras, I., Frise, E., Kaynig, V., Longair, M., Pietzsch, T., Preibisch, P., Rueden Saalfeld, S., Schmid, B., Tinevez, J.-Y., James White, D.J., Hartenstein, V., Eliceiri, K., Tomancak, P., Cardona, A., 2012. Fiji: an open-source platform for biological-image analysis. Nat. Methods 9 (7), 676–682.
Silin, D., Patzek, T., 2006. Pore space morphology analysis using maximal inscribed spheres. Physica A 371, 336–360.
Silin, D., Patzek, T., 2009. Predicting relative-permeability curves directly from rock images. SPE Annual Technical Conference and Exhibition. Society of Petroleum Engineers Society of Petroleum Engineers.
Silin, D., Tomutsa, L., Benson, S.M., Patzek, T.W., 2011. Microtomography and pore-scale modeling of two-phase fluid distribution. Transport Porous Media 86 (2), 495–515.
Steefel, C.I., Molins, S., Trebotich, D., 2013. Pore scale processes associated with subsurface CO2 injection and sequestration. Rev. Mineral. Geochem. 77 (1), 259–303.
Tokunaga, T.K., Wan, J., Jung, J.W., Kim, T.W., Kim, Y., Dong, W., 2013. Capillary pressure and saturation relations for supercritical CO2 and brine in sand: high-pressure Pc(Sw) controller/meter measurements and capillary scaling predictions. Water Resour. Res. 49, 4566–4579.
Tomasi, C., Maduchi, R., 1998. Bilateral filtering for gray and color images. 6th International Conference on Computer Vision, New Delhi, India 839–846.
Toussaint, R., Maloy, K.J., Meheust, Y., Lavoll, G., Jankov, M., Shafer, G., Schmittbuhl, J., 2012. Two-phase flow: structure, upscaling, and consequences for macroscopic transport properties. Vadose Zone J. 11 (3).
Voltolini, M., Zandomeneghi, D., Mancini, L., Polacci, M., 2011. Texture analysis of volcanic rock samples: quantitative study of crystals and vesicles shape preferred orientation from X-ray microtomography data. J. Volcanol. Geotherm. Res. 202 (1–2), 83–95.
Wang, S., Tokunaga, T.K., 2015. Capillary pressure- saturation relations for supercritical CO2 and brine in limestone/dolomite sands: implications for geologic carbon sequestration in carbonate reservoirs. Environ. Sci. Technol. 49, 7208–7217.
Weitkamp, T., Haas, D., Wegrzynek, D., Rack, A., 2011. ANKAphase: software for single-distance phase retrieval from inline X-ray phase contrast radiographs. J. Synchrotron Radiat. 18 (4), 617–629.
White, J.E., 1975. Computed seismic speeds and attenuation in rocks with partial gas saturation. Geophysics 40, 224–232.
Wilkinson, D., Willemsen, J.F., 1983. Invasion percolation: a new form of percolation theory. J. Phys. A: Math. Gen. 16 (14), 3365.
Wu, Y., Ajo-Franklin, J.B., Spycher, N., Hubbard, S.S., Zhang, G., Williams, K.H., Taylor, J., Fujita, Y., Smith, R., 2011. Geophysical monitoring and reactive transport modeling of ureolytically-driven calcium carbonate precipitation. Geochem. Trans. 12 (1), 7.
Wyckoff, R.T., Botset, H.G., 1936. The flow of gas-liquid mixtures through unconsolidated sands. J. Appl. Phys. 7 (9), 325–345.
Zambrano, M., Tondi, E., Mancini, L., Arzilli, F., Lanzafame, G., Materazzi, M., Torrieri, S., 2017. 3D Pore-network quantitative analysis in deformed carbonate grainstones. Mar. Petrol. Geol. 82, 251–264.
Zandomeneghi, D., Voltolini, M., Mancini, L., Brun, F., Dreossi, D., Polacci, M., 2010. Quantitative analysis of X-ray microtomography images of geomaterials: application to volcanic rocks. Geosphere 6 (6), 793–804.
Zuo, L., Ajo-Franklin, J.B., Voltolini, M., Geller, J.T., Benson, S.M., 2017. Pore-scale multiphase flow modeling and imaging of CO_2 exsolution in Sandstone. J. Petrol. Sci. Eng. 155, 63–77.